Search for the Chargino-Neutralino Pair Production Using Like-Sign Dilepton Events in 1.96-TeV Proton-Antiproton Collisions

(重心系エネルギー 1.96TeV 陽子・反陽子衝突実験における
同符号 2 レプトン事象を用いた
チャージーノ・ニュートラリーノ対生成の探索)

理学研究科

数物系専攻

プラドウ　スラキア

Search for the Chargino-Neutralino Pair Production Using Like-Sign Dilepton Events in 1.96-TeV Proton-Antiproton Collisions

A dissertation submitted
in partial fullfillment of the requirements
for the Degree of Master of Philosophy in Science
in the Graduate School of Science of
Osaka City University

by
Master Surakiat Puraduk

February 17th, 2012

Abstract

The collider Tevatron, which is located at the Fermi National Accelerator Laboratory in Batavia, Illinois(USA), ceased operations on 30 September, 2011. The Tevatron is the second highest energy particle collider in the world after the Large Hadron Collider(LHC). CDF is the experiment with the primary objective of the discovery of physics beyond the standard model.

In elementary particle physics, the standard model is the most popular theory which describes the phenomena of the elementary particles. But, the standard model have several unsolved theoretical problems. Supersymmetry is one of the candidates for the possible solutions to the problems. If we accept the supersymmetry, the superpartners, which are new particles introduced by the theory, are thought to exist. Furthermore, there are some supersymmetry models as to assumption of way to supersymmetry breaking. The superpartner productions have strong the model and parameter dependence. Therefore, the superpartner mass, branching ratio, etc. change due to the variety of the way to employ models, or set parameters.

This thesis is described search for the superpartner Chargino and Neutralino pair production using high-p_T isolated like-sign(LS) dilepton events as the bellow process,

$$qq' \to \tilde{\chi}_1^{\pm}\tilde{\chi}_2^0 \to \ell^{\pm}\ell^{\ell} + X.$$

The search is performed on a data collected by the CDF corresponding to an integrated luminosity of 8.5 fb^{-1}. For the minimal supergravity(mSUGRA) model, we estimated the sensitivities of variety parameter settings using Monte Carlo(MC) simulations.

The Boosted Decision Tree(BDT) are employed to get more search sensitivity in this analysis. The BDT is based on a multivariate analysis technique and used to separate the signal and background events in the final sample passing LS dilepton requirement.

There are no significant disagreement between data and background estimations in the BDT results. Then, the upper limits on the production cross-section for the chargino-neutralino can be set. As the result, we can exclude the region of $M_{\tilde{\chi}_1^{\pm}} < 120\mathrm{GeV}/c^2$ for the setting of mSUGRA parameters $(M_0,\ A_0,\ \tan\beta,\ \mathrm{sign}(\mu)) = (60GeV/c^2,\ 0,\ 5.0,\ +)$.

Acknowledgments

In writing this thesis, I am deeply grateful to everyone who supported and encouraged me. I could not have finished this thesis without the great help and support of the peaple around me.

Firstly, I would like to thank everyone in the Osaka City University high energy physics lab, especially Prof. Yoshihiro Seiya, Prof. Kazuhiro Yamamoto, Dr. Takayuki Wakisaka, and Dr. Daisuke Yamato. They were always making time for me in their very busy schedele, and gave me lots of advice for this study. In addition, they helped me in not only physics but also personal matters. I would like to express my gratitude to Prof. emeritus Toru Okusawa. He provided many useful comments to me.

Special thanks also to Dr. Atsunari Hamaguchi, my classmates Takashi Nakai and Kazuya Nakajima. They listened to my sufferings in aspect of life. Because of that, my mind is relaxed always. I want to thank the graduates Kazuaki Tshiro, Chie Matsumura and Shoji Yamamoto. I was very happy to spend few years at university with them.

Finally, I would like to thank my friends and family, especially my mother for her unconditional support over the past few years.

Contents

List of Figures

List of Tables

Chapter1

The Standard Model

The standard model(SM) is the most widely accepted particle physics theory, which describes the phenomena and proparties of the elementary particles, and was also tested by various experiments. The SM is based on the gauge field theory which is invariance under the gauge transformation. The SM can form three gauge field theories in the framework. The three gauge theories are "Quantum Electrodynamics(QED)", "Quantum Chromodynamics(QCD)" and "Weak theory". The QED describes the electromagnetic interaction between charged particles based on the $U(1)$ gauge group. The QCD describes the strong interaction between quarks and gluons based on the $SU(3)_C$ gauge group. And the Weak theory describes weak interaction where in the nuclei based on the $SU(2)$ gauge group. In particular, the QED and Weak theory are unified in the SM framework as $SU(2)_L \otimes U(1)_Y$ gauge theory. In addition, the "Higgs Mechanism" plays to give "Mass" to a particle with keeping the gauge invariance in the theory. This chapter describes the SM in detail.

1.1 Elementary Particles

The elementary particles in the SM are classified into two main categories: "Fermion" and "Boson". The Fermions construct matters in the universe, while the Bosons mediate forces between the elementary particles. The visible complex matters in this world are made up of them. This section goes into details of the elementary particles in the SM.

1.1.1 Fermion

The fermions are elementary particles with half-integral spin which obeys the "Pauli Exclusion Principle". The fermions are classified according to how they interact or equivalently, by what charges they carry. There are six quarks(up, down, charm, strange, top, bottom), and six leptons(electron, electron neutrino, muon, muon neutrino, tau, tau neutrino). Pairs from each classification are grouped together to form a generation, with corresponding particles exhibiting similar physical behavior. Table1.1 shows the list of the quarks and the leptons.

Fermion	**Generation**			**Charge**	**Isospin**
	I	**II**	**III**	$(Q/\|e\|)$	
Lepton	$\begin{pmatrix} \nu_e \\ e^- \end{pmatrix}_L$	$\begin{pmatrix} \nu_\mu \\ \mu^- \end{pmatrix}_L$	$\begin{pmatrix} \nu_\tau \\ \tau^- \end{pmatrix}_L$	$\begin{pmatrix} 0 \\ -1 \end{pmatrix}$	$\begin{pmatrix} +\frac{1}{2} \\ -\frac{1}{2} \end{pmatrix}$
	e_R	μ_R	τ_R	-1	0
Quark	$\begin{pmatrix} u \\ d \end{pmatrix}_L$	$\begin{pmatrix} c \\ s \end{pmatrix}_L$	$\begin{pmatrix} t \\ b \end{pmatrix}_L$	$\begin{pmatrix} +\frac{2}{3} \\ -\frac{1}{3} \end{pmatrix}$	$\begin{pmatrix} +\frac{1}{2} \\ -\frac{1}{2} \end{pmatrix}$
	u_R	c_R	t_R	$+\frac{2}{3}$	0
	d_R	s_R	b_R	$-\frac{1}{3}$	0

Table 1.1: List of the fermions(quarks and leptons) in the SM.

Interaction	**Gauge Boson** (symbol)	**Spin**	**Charge** $(Q/\|e\|)$	**Mass** (GeV/c^2)	**Effective coupling**
Electromagnetic	γ	1	0	0	1/137
Weak	Z^0	1	0	91.2	10^{-5}
Weak	$W^\pm$	1	± 1	80.4	10^{-5}
Strong	g	1	0	0	~ 1

Table 1.2: Summary of the forces and gauge boson in the SM.

1.1.2 Boson

The bosons play a role in mediating force between the elementary particles corresponding to type of forces. Such bosons are especially called "gauge boson". In the present, it is believed that there are at least 4 kind of force, "Electromagnetic", "Weak", "Strong" and "Gravity". The Gravity force is excluded in the SM due to normalization problem, and its extremely small affect in the partial world. The electromagnetic forces are propageted via "photon" by feeling electric charge which is gauge boson in the electromagnetic field. The weak force in teractions are mediated by $W^\pm$ and Z^0 bosons, unlike electromagnetic force, it can effect within short range($\sim 10^{-16}$cm). The strong force interactions are occured by exchangeing gauge boson so-called "gluon" via color charge. The force mediating particles, i.e. gauge bosons, are shown in Table1.2.

1.2 The $U(1)$ Theory : Quantum Electrodynamics

Quantum Electrodynamics(QED) is an abelian gauge theory with the group $U(1)$. The gauge field, which mediates the interaction between the charged 1/2 spinfields, is the electromagnetic field. The Lagrangian for a free field is given by

$$\mathscr{L} = \bar{\psi}(i\gamma^\mu \partial_\mu - m)\psi \tag{1.1}$$

The Lagrangian is invariant under the phase transformation,

$$\psi \to e^{i\alpha}\psi \tag{1.2}$$

where α is a real constant. Using Neother's theorem, this invariant implies the existance of a conserved current and charge.

$$\partial_\mu j^\mu = 0,\ j^\mu = -e\bar{\psi}\gamma^\mu\psi,\ Q = \int d^3x j^0 \tag{1.3}$$

In addition, the local gauge transformation is generalized as

$$\psi \to e^{i\alpha(x)}\psi, \tag{1.4}$$

where $\alpha(x)$ depends on space and time in a completely arbitrary way. Now, the Lagrangian(1.1) is not invariant under such phase transformation. Using(1.4),

$$\bar{\psi} \to e^{i\alpha(x)}\bar{\psi}, \tag{1.5}$$

the last term of the Lagrangian is invariant, however the term of derivative ψ is not as follows,

$$\partial_\mu\psi \to e^{i\alpha(x)}\partial_\mu\psi + ie^{i\alpha(x)}\psi\partial_\mu\alpha, \tag{1.6}$$

and the $\partial_\mu\alpha$ term breaks the invariant of the Lagrangian. To impose invariance of the Laglangian under local gauge transformation, the derivative ∂_μ is modified as D_μ, the treatment coveriantly transforms the Lagrangian under the phase transformation,

$$D_\mu\psi \to e^{i\alpha(x)}D_\mu\psi, \tag{1.7}$$

$$D_\mu \equiv \partial_\mu - ieA_\mu, \tag{1.8}$$

where a vector field A_μ is introduced to cancel the unwanted term in (1.6), and the vector field transforms as,

$$A_\mu \to A_\mu + \frac{1}{e}\partial_\mu\alpha. \tag{1.9}$$

Invariance of the Lagrangian(1.1) under the local gauge transformation(1.4) is achieved by replacing ∂_μ by D_μ,

$$\begin{aligned}\mathscr{L} &= i\bar{\psi}\gamma_\mu D^\mu\psi - m\psi\bar{\psi} \\ &= \bar{\psi}(i\gamma^\mu\partial_\mu - m)\psi + e\bar{\psi}\gamma^\mu\psi A_\mu.\end{aligned} \tag{1.10}$$

By demanding local phase invariance, it forces to introduce a vector field A_μ, i.e. gauge field QED. If the additional field is regarded as the physical photon field, the Lagrangian is added a term corresponding to its kinetic energy. Since the kinetic term must be invariant under(1.9), it can only involve the gauge invariant field strength tensor

$$F_{\mu\nu} = \partial_\mu A_\mu - \partial_\nu A_\mu. \tag{1.11}$$

Finally, the Lagrangian of QED is expressed as follows,

$$\mathscr{L} = \bar{\psi}(i\gamma^\mu\partial_\mu - m)\psi + e\bar{\psi}\gamma^\mu\psi A_\mu - \frac{1}{4}F_{\mu\nu}F^{\mu\nu}. \tag{1.12}$$

The addition of mass term $(1/2)m^2A_\mu A^\mu$ is prohibited by gauge invariance. The gauge particle must be massless and the gauge field can propagate to an infinite range.

1.3 The $SU(3)_C$ Theory : Quantum Chromodynamics

Quantum Chromodynamics(QCD) is the gauge theory for strong interactions. QCD is based on the extension of the QED idea, however it has a gauge transformation invariant under $SU(3)$ group on quark color fields. The Lagrangian is written in the following,

$$\mathscr{L} = \bar{q}_j(i\gamma^\mu\partial_\mu - m)q_j, \tag{1.13}$$

where $q_j(j = 1, 2, 3)$ denotes the three color fields. The Lagrangian(1.13) is to be invariant under local phase transformations as follows,

$$q(x) \to Uq(x) \equiv e^{i\alpha_a(x)T_a}q(x), \tag{1.14}$$

where U is an arbitrary 3×3 unitary matrix, it has the summation over the repeated suffix a. $T_a(a = 1, \cdots, 8)$ is a set of linearly independent traceless 3×3 matrices, and α_a are the group parameters. The group is non-Abelian since the generators T_a do not commute with each other,

$$[T_a, T_b] = if_{abc}T_c, \tag{1.15}$$

where f_{abc} are real constants called the structure constants of the group. To impose $SU(3)$ local gauge invariance on the Lagrangian(1.13), the infinitesimal phase transformation is introduced,

$$q(x) \to [1 + i\alpha_a(x)T_a]q(x), \tag{1.16}$$

$$\partial_\mu q \to (1 + i\alpha_a T_a)\partial_\mu q + iT_a q\partial_\mu\alpha_a. \tag{1.17}$$

The last term spoils the invariance of Lagrangian. The 8 gauge fields G^a_μ are constructed by requiring the invariance of the Lagrangian under the local gauge transformation,

$$G^a_\mu \to G^a_\mu - \frac{1}{g}\partial_\mu\alpha_a - f_{abc}\alpha_b G^c_\mu, \tag{1.18}$$

and form a covariant derivative,

$$D_\mu = \partial_\mu + igT_a G^a_\mu. \tag{1.19}$$

The gauge invariant QCD Lagrangian is formed by the replacement $\partial_\mu \to D_\mu$ in the Lagrangian(1.13), and adding a gauge invariant kinetic energy term for each of the G^a_μ fields,

$$\mathscr{L} = \bar{q}(i\gamma^\mu\partial_\mu - m)q - g(\bar{q}\gamma^\mu T_a q)G^a_\mu - \frac{1}{4}G^a_{\mu\nu}G^{\mu\nu}_a, \tag{1.20}$$

$$G^a_{\mu\nu} = \partial_\mu G^a_\nu - \partial_\nu G^a_\mu - gf_{abc}G^b_\mu G^c_\nu, \tag{1.21}$$

(1.20) is the Lagrangian for interacting colored quarks q and vector gluons G_μ, with coupling specified by g. The local gauge invariance requires the gluons to be massless. The field strength $G^a_{\mu\nu}$ has a remarkable new property as shown in the last term in (1.21). Imposing the gauge symmetry has required that the kinetic energy term in Lagrangian is not purely kinetic but includes an induced self-interaction between the gauge bosons and reflects the fact that gluons themselves carry color charge.

1.4 The $SU(2)_Y \otimes U(1)_Y$ Theory : Electroweak Theory

The electroweak theory is a gauge theory unified the electromagnetic $U(1)$ and weak interactions $SU(2)$. The weak interaction typically occurs in β decay in nuclei($n \to p + \ell + \nu_\ell$) via a W boson which is weak gauge boson. The weak interaction acts only left-handed fermions, so-called $V - A$ structure, and based on $SU(U)$ isospin group with three vector bosons. The electroweak theory is suggested by Glashow, Weinberg, and Salam.

By demanding weak interaction, the quark fields are expressed as follows,

$$\psi_L = \begin{pmatrix} q_u \\ q_d \end{pmatrix}_L, \psi_R = q_R. \tag{1.22}$$

The left-handed quark fields can be expressed in doublets, while the right-handed quark fields in singlets, where q_u is up-type quarks(u, c, t), q_d is down-typ quarks(d, s, b), and q_R is six quark flavours(u, d, c, s, t, b). The lepton fields are also expressed by,

$$\psi_L = \begin{pmatrix} \nu_\ell \\ \ell^- \end{pmatrix}_L, \psi_R = l_R. \tag{1.23}$$

where ℓ means three lepton flavours i.e. μ, and τ. Note that there are no right-handed neutrino fields due to satisfying $V - A$ structure in the weak interaction. Here, the free Lagrangian for the lepton and quark fields is written in,

$$\mathscr{L} = \sum_{j=L,R} i\bar{\psi}_j \gamma^\mu \partial_\mu \psi_j. \tag{1.24}$$

The Lagrangian(1.24) is invariant under global transformation,

$$\psi_L \to e^{i\alpha_a T^a + i\beta Y} \psi_L, \tag{1.25}$$

$$\psi_R \to e^{i\beta Y} \psi_R, \tag{1.26}$$

where the parameter Y is hypercharge for $U(1)_Y$ phase transformation, the T^0 is defined by using Paunli matrices as follows,

$$T^0 = \frac{\tau^0}{2},\ \tau^1 = \begin{pmatrix} 0 & 1 \\ 1 & 0 \end{pmatrix},\ \tau^2 = \begin{pmatrix} 0 & -i \\ i & 0 \end{pmatrix},\ \tau^3 = \begin{pmatrix} 1 & 0 \\ 0 & -1 \end{pmatrix}, \tag{1.27}$$

and it is under $SU(2)_L$ transformation. The Lagrangian should be invariant under local $SU(2)_L \otimes U(1)_Y$ gauge transformation,

$$\psi_L \to e^{i\alpha_a(x) T^a + i\beta(x) Y} \psi_L, \tag{1.28}$$

$$\psi_R \to e^{i\beta(x) Y} \psi_R. \tag{1.29}$$

To achieve the local gauge invariance in the Laglangian, the derivative is replaced by covariant derivatives,

$$D_{\mu L} \equiv \partial_\mu + igT_a W_\mu^a + i\frac{g'}{2} B_\mu Y, \tag{1.30}$$

$$D_{\mu R} \equiv \partial_\mu + i\frac{g'}{2} B_\mu Y, \tag{1.31}$$

$D_{\mu L}(D_{\mu R})$ is for the left(right)-handed fermion fields, g is the coupling constant of $SU(2)_L$ and g' is of $U(1)_Y$. The covariant derivatives have gauge fields, $W^a_\mu (a = 1, 2, 3)$ for $SU(2)_L$, and B_μ for $U(1)_Y$. The gauge fields also transform as,

$$B_\mu \rightarrow B_\mu - \frac{1}{g'}\partial_\mu \beta, \tag{1.32}$$

$$\mathbf{W}_\mu \rightarrow \mathbf{W}_\mu - \frac{1}{g}\partial_\mu \boldsymbol{\alpha} - \boldsymbol{\alpha} \times \mathbf{W}_\mu. \tag{1.33}$$

In addition, the gauge field strength tensors are introduced by requiring the local gauge invariant,

$$B_{\mu\nu} \equiv \partial_\mu B_\nu - \partial_\nu B_\mu, \tag{1.34}$$

$$W^a_{\mu\nu} \equiv \partial_\mu W^a_\nu - \partial_\nu W^a_\mu - g\upsilon_{abc} W^b_\mu W^c_\nu. \tag{1.35}$$

Finally, the Lagrangian under gauge invariant in electroweak interaction can be written as,

$$\mathscr{L} = \sum_{j=L,R} i\bar{\psi}_j \gamma^\mu D_{\mu j} \psi_j - \frac{1}{4} W^a_{\mu\nu} W^{\mu\nu}_a - \frac{1}{4} B_{\mu\nu} B^{\mu\nu}, \tag{1.36}$$

Although the weak and electromagnetic interactions coexist in the $SU(2)_L \otimes U(1)_Y$ gauge symmetry, it describes no realistic world, because there are no mass term for fermions and weak gauge bosons which are known that they are massive, and weak interaction only affects in short range. However introducing the mass terms such as $\frac{1}{2} M^2_W W_\mu W^\mu$ in Lagrangian breaks the gauge symmetry. The fermion terms also break due to different transformation between the left-handed and right-handed fermion fields,

$$m_f \bar{f} f = m_f (\bar{f}_R f_L + \bar{f}_L f_R), \tag{1.37}$$

using the left-handed and right-handed relation equations,

$$f_L = \frac{1}{2}(1 - \gamma^5) f, \;\; f_R = \frac{1}{2}(1 + \gamma^5) f. \tag{1.38}$$

Fortunately, the nature have a solution(mechanism) to be invariant under gauge transformation when the Lagrangian has a mass terms for fermion and weak gauge boson, so-called "Spontaneous symmetry breaking".

1.5 Spontaneous Symmetry Breaking

To give mass to the gauge bosons and fermions, the electroweak gauge symmetry are hidden. Here let us start by introducing the scalar real field ϕ as simple example, and its Lagrangian is written by,

$$\mathscr{L} = \frac{1}{2}\partial_\mu \phi \partial^\mu \phi - V(\phi), \tag{1.39}$$

$$V(\phi) = \frac{1}{2}\mu^2 \phi^2 + \frac{1}{4}\lambda \phi^4, \tag{1.40}$$

where $\lambda > 0$, the Lagrangian is invariant under the symmetry operation: $\phi \to -\phi$.

If $\mu^2 > 0$, it can be regarded that the Lagrangian describes a scalar fields with mass μ, the ϕ^4 terms means self-interaction with coupling λ, and the minimum of the potential $V(\phi)$ is,

$$\langle 0|\phi|0\rangle \equiv \phi_0 = 0, \tag{1.41}$$

as shown in the left side of Figure1.1. On the other hand, if $\mu^2 < 0$, the potential $V(\phi)$ has a minimum when,

$$\frac{\partial V}{\partial \phi} = \mu^2\phi + \lambda\phi^3 = 0, \tag{1.42}$$

$$\langle 0|\phi^2|0\rangle \equiv \phi_0^2 = -\frac{\mu^2}{\lambda} \equiv v^2, \tag{1.43}$$

as shown in the right side of Figure1.1. The value $v = \sqrt{\mu^2/\lambda}$ is called "vacuum expectation value(VEV)" of the scalar feild ϕ. Here the field ϕ is expanded around the minimum value v with the quantum fluctuation η,

$$\phi = v + \eta. \tag{1.44}$$

From this, the Lagrangian(1.40) becomes

$$\mathscr{L} = \frac{1}{2}\partial_\mu\eta\partial^\mu\eta - \lambda v\eta^3 - \frac{1}{4}\eta^4 + \text{const}, \tag{1.45}$$

where a scalar field η with mass $m_\eta = \sqrt{-2\mu^2}$ appears in the Lagrangian(1.45), and there are self-interaction terms η^3 and η^4, in particular, the cubic term breaks the symmetry in the Lagrangian without external operation, it is called "Spontaneous Symmetry Breaking(SSB)".

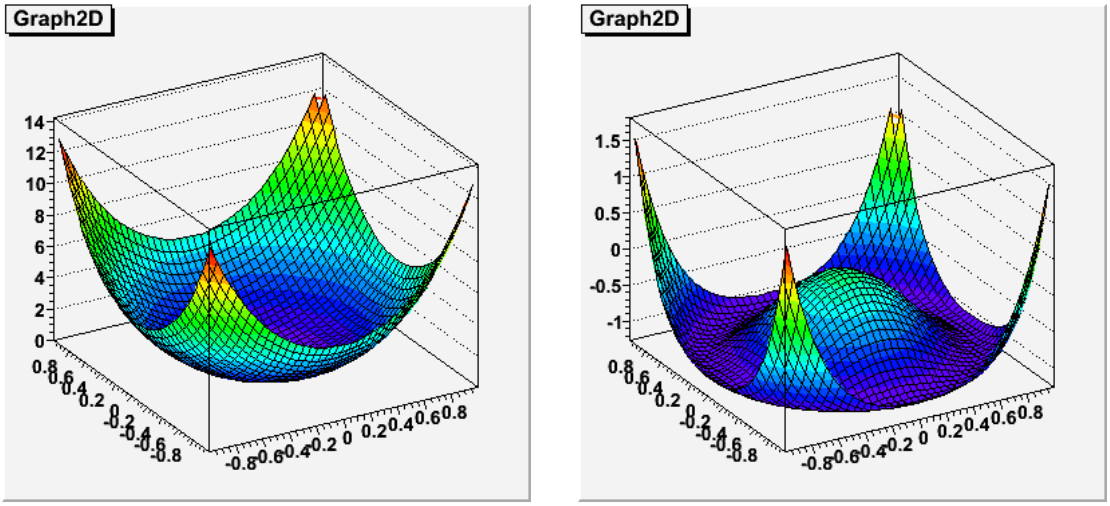

Figure 1.1: The potential $V(\phi)$ of the scalar field ϕ for $\mu^2 > 0$(left) and $\mu^2 < 0$(right).

1.6 Higgs Mechanism

However the Laglangian(1.36) is invariant under local gauge invaritant, the Lagrangian describes the no real world picture because the weak gauge bosons and fermions have no mass in the Lagrangian. But the Lagrangian is broken by including the mass term. Now, let us show that the Lagrangian becomes the real world Lagrangian by using the symmetry breaking. By introducing complex scalar doublet,

$$\phi = \begin{pmatrix} \phi^+ \\ \phi^- \end{pmatrix} = \frac{1}{\sqrt{2}} \begin{pmatrix} \phi_1 + i\phi_2 \\ \phi_3 + i\phi_4 \end{pmatrix}, \ Y_\phi = +1, \tag{1.46}$$

where the hypercharge is 1 for the scalar fields, the Lagrangian can be written by

$$\mathscr{L} = (\partial_\mu \phi)^\dagger (\partial^\mu \phi) - \mu^2 \phi^\dagger \phi - \lambda (\phi^\dagger \phi)^2. \tag{1.47}$$

In this case, if $\mu^2 < 0$, the VEV and the scalar field after the symmetry breaking with the real scalar field h become as follows,

$$\phi^\dagger \phi = \frac{\phi_1^2 + \phi_2^2 + \phi_3^2 + \phi\ 2_4}{2} = \frac{-\mu^2}{2\lambda} \equiv \frac{v^2}{2}, \tag{1.48}$$

$$\phi = \frac{1}{\sqrt{2}} \begin{pmatrix} 0 \\ v + h \end{pmatrix}, \tag{1.49}$$

where the scalar fields are chosen as $\phi^1 = \phi^2 = \phi^4 = 0$, and $\phi^3 = v$. Let us expand the first term of the Lagrangian(1.47), i.e. the kinematical terms,

$$\begin{aligned} |D_\mu \phi|^2 &= |(\partial_\mu - igT^a W_\mu^a + i\frac{g'}{2} B_\mu)\phi|^2 \\ &= \frac{1}{2}(\partial_\mu h)^2 + \frac{g^2 v^2}{4} |\frac{W_\mu^1 + iW_\mu^2}{2}| + \frac{v^2}{8} |gW_\mu^3 - g' B_\mu|^2 + (\text{interaction terms}), \end{aligned} \tag{1.50}$$

where the derivative is replaced to covariant derivative(1.31), and the define the field $W_\mu^\pm$, Z_μ and A_μ written as follows,

$$W_\mu^\pm = \frac{1}{\sqrt{2}}(W_\mu^1 \pm iW_\mu^2), \tag{1.51}$$

$$Z_\mu = W_\mu^3 \cos\theta_W - B_\mu \sin\theta_W, \tag{1.52}$$

$$A_\mu = W_\mu^3 \sin\theta_W + B_\mu \cos\theta_W, \tag{1.53}$$

where weak mixing angle θ_W is defined as $g' = g\tan\theta_W$, the A_μ field is the orthogonal field to the Z_μ field, and the masses of fields can be expressed as respectively,

$$M_W = \frac{1}{2} vg, \ M_Z = \frac{1}{2} v\sqrt{g^2 + g'^2}, \ M_A = 0. \tag{1.54}$$

Note that the W_μ and the Z_μ fields becom massive, while the A_ν field is still massless, that is , the weak gauge bbosons can have desirable mass by introducing the SSB, in

particular, it is called "Higgs Mechanism". By using the weak mixing angle θ_W, the θ_μ field is related to Z_μ field as follows,

$$M_W = M_Z \cos\theta_W. \tag{1.55}$$

The fermion fields should be massive to achieve the true world in the electroweak Lagrangian. The Higgs mechnism also gives a mass to the fermions under the local gauge invariant. The Lagrangian with fermion fields is written by,

$$\mathscr{L}_{Yukawa} = -G_f \bar{\psi}_L \phi \psi_R - G_f \bar{\psi}_R \phi^\dagger \psi_L, \tag{1.56}$$

where G_f is arbitrary constant for each fermion. First, the lepton sector Lagrangian becomes,

$$\begin{aligned} \mathscr{L} &= -G_\ell[(\bar{\nu}_\ell, \bar{\ell})_L \begin{pmatrix} \psi^+ \\ \psi^0 \end{pmatrix} \ell_R + \bar{\ell}_R(\psi^-, \bar{\psi}^0) \begin{pmatrix} \nu_\ell \\ \ell \end{pmatrix}] \\ &= -\frac{G_\ell}{\sqrt{2}} v(\bar{\ell}_L \ell_R + \bar{\ell}_R \ell_L) - \frac{G_\ell}{\sqrt{2}}(\bar{\ell}_L \ell_R + \bar{\ell}_R \ell_L) h \\ &= -m_\ell \bar{\ell}\ell - \frac{m_\ell}{v}\bar{\ell}\ell h, \end{aligned} \tag{1.57}$$

using (1.38) and $m_\ell = G_\ell v/\sqrt{2}$ is defined as the lepton mass. The lepton sector Lagrangian(1.57) then keeps the gauge symmetry under the local transformation. Let us show that the quark sector Lagrangian also becomes the invariant. In the quark sector, the new higgs doublet must be introduced by using ϕ to give the up-type quark mass,

$$\phi_c = i\tau_2 \phi = \begin{pmatrix} -\bar{\phi}^0 \\ \phi^- \end{pmatrix}, \tag{1.58}$$

the higgs doublet is chosen the following after the symmetry breaking,

$$\phi_c = \frac{1}{\sqrt{2}} \begin{matrix} v+h \\ 0 \end{matrix} \quad (). \tag{1.59}$$

The quark sector Lagrangian is formed by

$$\begin{aligned} \mathscr{L}_{quark} &= -G_d(\bar{u}, \bar{d})_L \begin{pmatrix} \psi^+ \\ \psi^0 \end{pmatrix} d_R - G_u(\bar{u}, \bar{d})_L \begin{pmatrix} -\psi^0 \\ \psi^- \end{pmatrix} u_R + h.c. \\ &= -m_d \bar{d}d - m_u \bar{u}u - \frac{m_d}{v}\bar{d}dh - \frac{m_u}{c}\bar{u}uh, \end{aligned} \tag{1.60}$$

where the down-type and up-type quark masses are defined as $m_d = G_d v/\sqrt{2}$ and $m_u = G_u v/\sqrt{2}$ respectively. The quark sector Lagrangian also preserves the gauge invariant after the symmetry breaking.

Chapter2

Supersymmetry

The SM is in well agreement with experimental measurements. But the SM contains several nagging theoretical problems which cannot be solved without the introduction of some new physics. Supersymmetry(SUSY) is one of the popular candidate for such new physics, which is a symmetry that relates elementary particles of one spin to other particles that differ by half a unit of spin and are known as "Superpartners".

2.1 A SUSY Toy Model

We have a hermitian Hamiltonian H and non-hermitian operators $Q, Q^\dagger$ related through the anti-commutor

$$H = \frac{1}{2}\{Q, Q^\dagger\} \equiv \frac{1}{2}(QQ^\dagger + Q^\dagger Q), \tag{2.1}$$

where the operators obey the following "$0+1$ dimensional SUSY algebra",

$$\{Q, Q\} = \{Q^\dagger, Q^\dagger\} = 0, \ [Q, H] = [Q^\dagger, H] = 0. \tag{2.2}$$

The Q and $Q^\dagger$ are called "supercharges" and generate supersymmetry transformation. It is a direct consequence of (2.2) that $Q^2 = Q^{\dagger 2} = 0$.

Now consider a Hilbert space $(\mathcal{H}, \langle|\rangle)$ carrying a representation of H, Q and $Q^\dagger$. From the algebra(2.2), it follows that H is positive definite,

$$\begin{aligned} 2\langle\psi|H|\psi\rangle &= \langle\psi|\{Q, Q^\dagger\}|\psi\rangle \\ &= \langle\psi|QQ^\dagger|\psi\rangle + \langle\psi|Q^\dagger Q|\psi\rangle \\ &= ||Q|\psi\rangle||^2 + ||Q^\dagger|\psi\rangle||^2 \geq 0. \end{aligned} \tag{2.3}$$

To further examine the state space, we diagonalise H and consider the eigenstates $|n\rangle$ sush that

$$H|n\rangle = E_n|n\rangle. \tag{2.4}$$

For the case of $E_n = E > 0$, we introduce the scaled operators $a = Q/\sqrt{2E}$ and $a^\dagger = Q^\dagger/\sqrt{2E}$ which, within the space of states of energy E, obey the algebra

$$\{a, a^\dagger\} = 1, \quad \{a, a\} = \{a^\dagger, a^\dagger\} = 0. \tag{2.5}$$

We now construct all the states with energy E, in analogy to the construction of harmonic oscillator states via creation operator acting on the vacuum. Again, we clearly have $a^2 = a^{\dagger 2} = 0$, from which it follows that the only eigenvalue of a is 0. Call the state with

this eigenvalue $|-\rangle$. We can create no more states by acting on this with a, and we can create only one more by acting $a^\dagger$(since $a^{\dagger 2} = 0$), which we call $|+\rangle \equiv a^\dagger|-\rangle$. Hence we have a subsystem two states obeying

$$a^\dagger|-\rangle = |+\rangle, \quad a|+\rangle = |-\rangle, \quad a|-\rangle = a^\dagger|+\rangle = 0. \tag{2.6}$$

A simple 2d representation of the algebra(2.5) is given by the following matrices and vectors,

$$a = \begin{pmatrix} 0 & 0 \\ 1 & 0 \end{pmatrix}, \; a^\dagger = \begin{pmatrix} 0 & 1 \\ 0 & 0 \end{pmatrix}, \; |+\rangle = \begin{pmatrix} 1 \\ 0 \end{pmatrix}, \; |-\rangle = \begin{pmatrix} 0 \\ 1 \end{pmatrix}. \tag{2.7}$$

We see here a basic example of the existence of two types in SUSY theories; "+" states and "−" states which will be "bosons" and "fermions". They are transformed into each other by the action of the SUSY generators, and more generally we will see that

$$Q|\text{boson}\rangle = |\text{fermion}\rangle, \quad Q|\text{fermion}\rangle = |\text{boson}\rangle, \tag{2.8}$$

and similarly for the action of $Q^\dagger$. We also have an example of the SUSY property that states of non-zero energy are degenerate and appear in "pairs".

We now turn to the states of zero energy, $H|0\rangle = 0$. Directly from (2.3), we must have

$$0 = ||Q|\psi\rangle||^2 + ||Q^\dagger|\psi\rangle||^2 \tag{2.9}$$

so that a vacuum state $|0\rangle$ exists if and only if

$$Q|0\rangle = Q^\dagger|0\rangle = 0. \tag{2.10}$$

2.2 SUSY Particles

According to the supersymmetry theory, each fermion should have a partner boson, the fermion's superpartner and each boson should have a partner fermion. Exact unbroken supersymmetry would predict that a particle and its superpartners would have the same mass. No superpartners of the Standard Model particles have yet been found. This may indicate that supersymmetry is incorrect, or it may also be the result of the fact that supersymmetry is not an exact, unbroken symmetry of nature. If superpartners are found, its mass would determine the scale at which supersymmetry is broken. Table 2.1 shows the superpartners for the SM elemenraty particles.

Furthermore, since neutral gaugino($\tilde{Z}^0$, $\tilde{B}^0$) and neutral Higgsino($\tilde{H}_1^0$, $\tilde{H}_2^0$) have equal quantum number, they create a state of neutralino($\tilde{\chi}_1^0$, $\tilde{\chi}_2^0$, $\tilde{\chi}_3^0$, $\tilde{\chi}_4^0$) by mixture. In a similar way, charged gaugino($\tilde{W}^\pm$) and charged Higgsino($\tilde{H}^\pm$) create chargino($\tilde{\chi}_1^\pm$, $\tilde{\chi}_2^\pm$) mixing state. The study discribed in this thesis is searching for the pair production of the mixing states chargino-neutralino.

SM elementary particle			SUSY particle		
spin	**name**	**symbol**	**spin**	**name**	**symbol**
$\frac{1}{2}$	**quarks :**	$(u,d)_L, u_R, d_R$ $(c,s)_L, c_R, s_R$ $(t,b)_L, t_R, b_R$	$\frac{1}{2}$	**squarks :**	$(\tilde{u},\tilde{d})_L, \tilde{u}_R, \tilde{d}_R$ $(\tilde{c},\tilde{s})_L, \tilde{c}_R, \tilde{s}_R$ $(\tilde{t},\tilde{b})_L, \tilde{t}_R, \tilde{b}_R$
$\frac{1}{2}$	**leptons :**	$(\nu_e,e)_L, e_R$ $(\nu_\mu,\mu)_L, \mu_R$ $(\nu_\tau,\tau)_L, \tau_R$	$\frac{1}{2}$	**sleptons :**	$(\tilde{\nu_e},\tilde{e})_L, \tilde{e}_R$ $(\tilde{\nu_\mu},\tilde{\mu})_L, \tilde{\mu}_R$ $(\tilde{\nu_\tau},\tilde{\tau})_L, \tilde{\tau}_R$
0	**higgs :**	$h, H, A, H^\pm$	$\frac{1}{2}$	**higgsino :**	$\tilde{H}_1^0, \tilde{H}_2^0, \tilde{H}^\pm$
1	**gluon :**	g	$\frac{1}{2}$	**gluino :**	$\tilde{g}$
1	**photon :**	γ	$\frac{1}{2}$	**bino :**	$\tilde{B}^0$
1	**weak bosons :**	$W^\pm, Z^0$	$\frac{1}{2}$	**wino :**	$\tilde{W}^\pm, \tilde{Z}^0$
2	**graviton :**	G	$\frac{3}{2}$	**gravitino :**	$\tilde{G}$

Table 2.1: List of the supersymmetric particles.

2.3 SUSY Answers

The problems in the SM that are left unsolved, are may fixed by introduction of SUSY. This following section describes the SM problems in some detail.

2.3.1 Hierarchy Probrem

The masses in the stadard model are generated by the Higgs boson. Experimentally, we have $M_h \sim 10^2$ GeV/c^2, but this is very sensitive to quantum corrections. The scalar potential for the Higgs boson h is given by,

$$V \sim M_{h_0}^2 h^2 + \lambda h^4. \tag{2.11}$$

At one loop, the quartic self-interactions of the Higgs boson(proportional to λ) generate a quadratically divergent contribution to the Higgs boson mass which must cancelled by the mass counterterm δM_h^2,

$$M_h^2 \sim M_{h0}^2 + \frac{\lambda}{4\pi^2}\Lambda^2 + \delta M_h^2. \tag{2.12}$$

The Λ is a cutoff, which is between the electroweak scale and the Planck scale in the SM. This leads to an unsatisfactory situation. The large quadratic contribution to the Higgs boson mass-squared, of $\mathcal{O}(10^{18}GeV)^2$, must be cancelled by the counterterm δM_h^2 that is roughly less than $(800GeV)^2$. This requires a cancellation of one part in 10^{16}. For the introduction of the SUSY, many Feynman diagrams contributing to mass corrections in SUSY theories cancel against other Feynman diagrams in which a particle loop is replaced by its superpartner loop. Reconsider the one loop contribution to the Higgs

boson in a theory which contaians both massive scalars ϕ, and fermions ψ, in addition to the Higgs field h. The Lagrangian is given by:

$$\mathscr{L} \sim -g_F \bar{\psi}\psi h - g_S^2 h^2 \phi^2. \tag{2.13}$$

If we again calculate the one-loop contribution to M_h^2 we find

$$\begin{aligned} M_h^2 \sim M_{h0}^2 \quad &+ \quad \frac{g_F^2}{4\pi^2}(\Lambda^2 + m_F^2) - \frac{g_S^2}{4\pi^2}(\Lambda^2 + m_S^2) \\ &+ \quad \text{logarithmic divergences} + \text{uninteresting terms.} \end{aligned} \tag{2.14}$$

The relative minus sign between the fermion and scalar contributions to the Higgs boson mass-squared is the well-known result of Fermi statistics. We see that if $g_S = g_F$ the terms which grow with Λ^2 cancel and we left with a well behave contribution to the Higgs boson mass so long as the fermion and scalar masses are not too different,

$$M_h^2 \sim M_{h0}^2 + \frac{g_F^2}{4\pi^2}(m_F^2 - m_S^2). \tag{2.15}$$

Attempt have been made to quantify "not too diferent". Figure 2.3.1 shows that the contribution from felmionic(t) and scalar($\tilde{t}$) squark often cancel exactly.

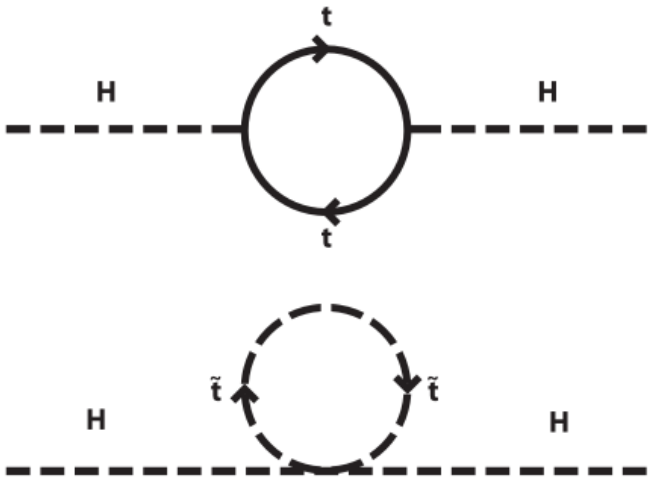

Figure 2.1: Cancellation of the Higgs boson quadratic mass renormalization.

2.3.2 Gauge Coupling Unification

The gauge coupling of the SM is $SU(3) \otimes SU(2) \otimes U(1)$. Various attempts have been made at constructing a grand unified theory(GUT). A unified theory would imply a

unified coupling: however, the couplings in the SM run as shown in the green-line of Figure 2.2, and do not appear to intersect. With SUSY, the couplings very nearly unify at the order of 10^{16}GeV.

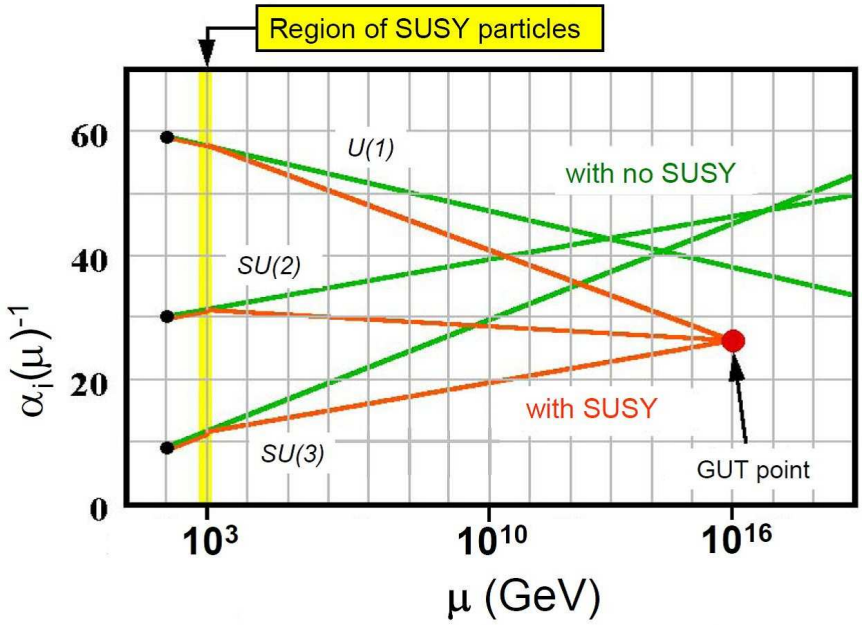

Figure 2.2: The strong, weak and electromagnetic couplings α^{-1} of the SM, for the case of with SUSY(red) and no SUSY(green).

2.3.3 Dark Matter

The energy content of the universe is roughly 4% ordinary matter, 22% dark matter and 74% dark energy. There are most likely a number of different constituents of dark matter. One of the most impotant candidates besides neutrinos is the "neutralino", the lightest particle of the minimal supersymmetric standard model(MSSM) yet to be found. The hope is that the Tevatron will find the neutralino.

2.4 Minimal Supergravity Model

Unbroken supersymmetry predicts that there are no mass differences within superpartners. Since the superpartners of the SM particles have not been observed, supersymmetry, if it exists, must be a broken symmetry, allowing the superpartners to be heavier than the corresponding SM particles. The SUSY is considered to break in a "hidden

sector", and we cannot know how SUSY is broken. There are some SUSY models For the assumption of how SUSY is broken spontaneously.

Minimal supergravity(MSUGRA) is one of the model with the assumption of SUSY breaking via gravitational interaction. In this model the SUSY productions are controled by only 5 parameters, as against over 100 parameters for the MSSM. The 5 parameters are,

- m_0 : Common scalar mass a Grand Unification Theory(GUT)
- $m_{1/2}$: Common gaugino mass at GUT
- A_0 : Common trilinear coupling at GUT
- $tan\beta$: Ratio of Higgs vacuum expectation values
- sign(μ) : Higgsino mass parameter sign

Figure 2.3 described the superpartner mass as a function of energy scale. Blue, red, black and green line in the figure each show the mass of squark, slepton, gaugino and Higgsino. At the GUT scale($\sim 10^{16}$GeV), the mass of scalar, gaugino and Higgsino are unified in m_0, $m_{1/2}$ and $(\mu^2 + m_0^2)$, respectively.

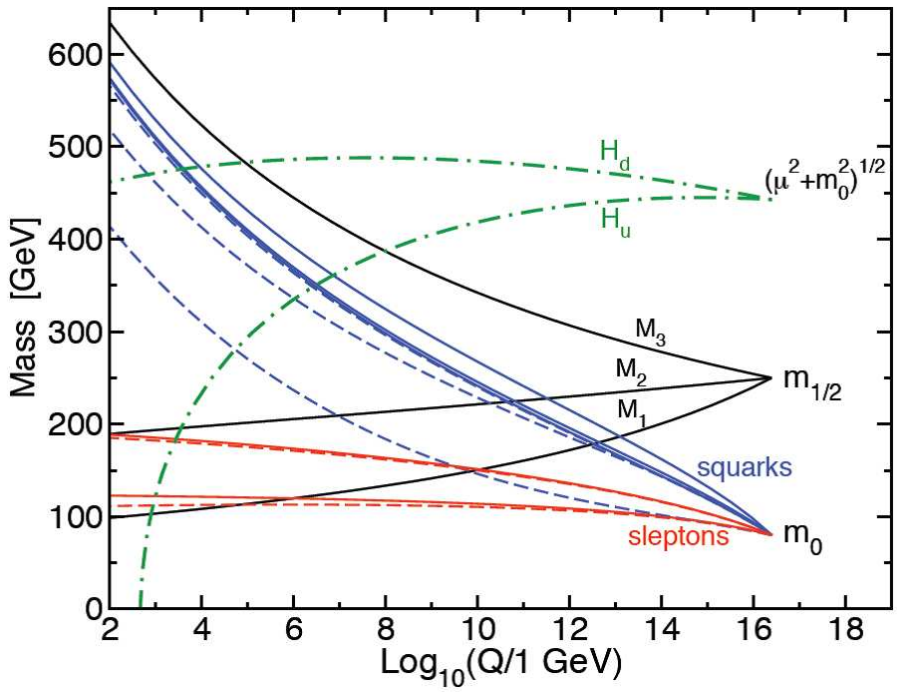

Figure 2.3: The superpartner mass as a function of energy scale for the mSUGRA model.

Chapter3

Experimental Apparatus

The CDF experiment that is main part of this thesis, is carried out with a circular particle accelerator Tevatron. The accelerator is located at the Fermi National Accelerator Laboratory in Batavia, Illinois, in the US. It provides proton-antiproton collisions with a center-of-mass energy of $\sqrt{s} = 1.96$TeV. There are two collision points in Tevatron ring, and detectors are installed in each points. One of the detectors is called The Collider Detector at Fermilab(CDF Ⅱ), the other is DØ. This study uses the former. The CDF RunⅡ experiment started in 2001, and continued until September, 2011. This chapter describes the proton-antiproton beam production, acceleration systems, the CDF Ⅱ detector design and etc.

3.1 The Accelerator Chain

In the collision experint described in this thesis, proton and antipron beams are used. The protons and antiprotons that are produced at each sources are accelerated to 980GeV. The design of an accelerator's chain is led by the consideration of the following requirements. One is that antiprotons must be produced and stored, Unlike protons that are abundant in nature. In addition, the proton and antiproton beams cannot be accelerated from rest to high energies by only single accelerator, because no magnets have the necessary dynamic range. Figure 3.1 shows an aerial photograph and a diagram of the Fermilab accelerator chain.

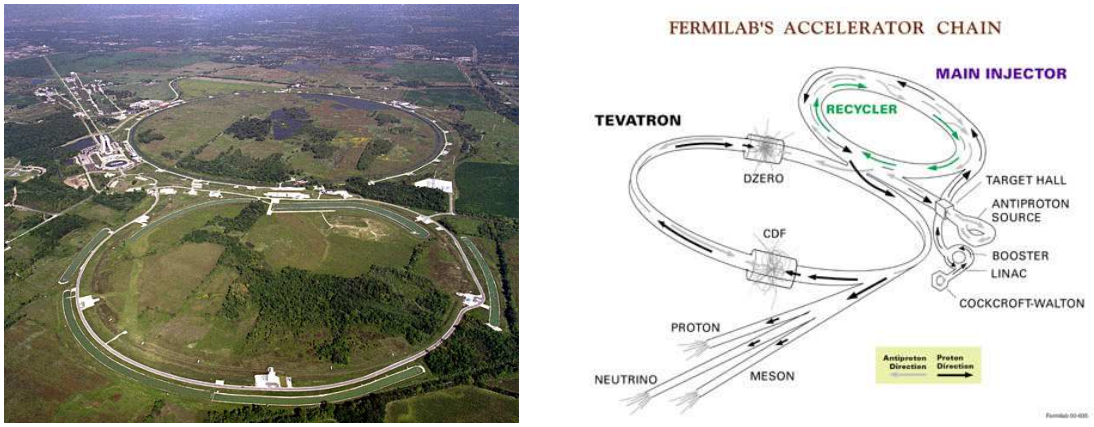

Figure 3.1: An air photo(right) and a diagram(left) of the Fermilab accelerator chain.

3.1.1 Proton Beam

The proton beams are available from H^+ ions that are made from ionized hydrogen gases. The H^+ ions are accelelated to 750keV of kinetic energy by Cockroft-Walton pre-accelerator in the first step. And then the ionized gases enter a linear accelerator(Linac) that is approximately 150m long, and are accelerated to 400MeV. The acceleration in the Linac is done by a series of "kicks" from Radio Frequency(RF) cavities.

The H^+ ions with 400MeV are injected into the Booster that is a circular synchrotron with approximately 150m diameter. At this time, electrons contained in the ionized hydrgen gases are removed by passing carbon foil, and pure protons are available. The resultant protons are accelerated from 400MeV to 8GeV by a series of magnets arranged around the synchrotron that interspersed with 18 RF cavities.

3.1.2 Antiproton Beam

The antiprotons are available from the protons on the way to produce proton beams. The protons of 120GeV are extracted from the Main injector, and strike a nickel target at the Antiproton Source. This produces spray of secondary particles that contain a trace of antiprotons. To select only antiprotons from tha spray, bending magnets that can choose particles momentum and charge are used. The resultant 8GeV antiprotons are directed into the Debuncher. About one antiproton is produced per 10^5 protons.

The Debuncher is a rounded triangular-shaped syncrotron with a mean radius of 90m. It can accept 8GeV antiprotons from the target station, and maintain the beam with an energy of 8GeV. Its primary purpose is to efficiently capture the high momentum spread antiprotons coming from the target using RF manipulation called bunch rotation which reduce the antiproton momentum spread. The reduction is done to improve the Debuncher to Accumlator transfer because of the limited momentum aperture of the Accumulator at injection.

The Accumulator which is also triangular-shaped syncrotron is mounted in the same tunnel as the Debuncher. It is the storage ring for antiprotons, all of the antiprotons that are made in the chain are stored here at 8GeV and cooled by the time use it.

3.1.3 Main Injector

The Main Injector(MI) is a circular synchrotron seven times the circumference of the Booster and slightly more than half the circumference of the Tevatron. The MI has 18 accelerating cavities. It can accelerate 8GeV protons from the Booster to either 120GeV or 150GeV, depending on either destination. When it is used to inject into the Tevatron, the final beam energy is 150GeV. As well as accepting protons from Booster, the MI can accept antiprotons from the Antiproton Source. The MI can accelerate beam as fast as every 2.2 seconds.

3.1.4 Recycler

The Recycler is an antiproton storage ring installed in the same tunnel as the MI. The proposed purpose of the Recycler was to recycle the antiprotons from a Tevatron store, cooling them and storing them alongside those sent from the Antiproton Source. This was abandoned after early problems in RunII. The Recycler now accepts transfers only from the Antiproton Source and cools them further than the antiprotons Accumulator is capable. The Recycler uses both a atochastic cooling system and an electron cooling system. Stochastic cooling is used to cool the beam in Recycler, but loses its effectiveness with higher intensities. Once acove 2×10^{12} antiprotons in the Recycler, electron cooling is required. Electron cooling works on the principle of momentum transfer between electrons and antiprotons, a highly concentrated, cool beam of electrons is driven at the same energy as the antiprotons and laid overtop of the antiprotons. The resulting glancing collisions between electrons and antiprotons transfer some of the momentum from the "hot" antiprotons to the "cool" electrons. With enough electrons, a substantial longitudinal cooling force is produced by absorbing momenta from the antiprotons allowing for more compact, brighter bunches to send to the Tevatron.

3.1.5 Tevatron

The Tevatron is a circular synchrotron with a approximately 2km diameter. In the final stage for the acceleration chain, the Tevatron receives protons and antiprotons from the MI and accelerates them from 150GeV to 980GeV. In Collider mode, the Tevatron can store beams for hours at a time. Because the Tevatron is primarily storage ring, the length of time between acceleration cycles is widely variable.

One of vital aspects of the Tevatron is the cryogenically cooled accelerator. The magnets in the Tevatron used associated with accelerations, which are made of superconducting materials. Therefore, the magnets need to be kept extremely cold($\sim$ 4K) to remain a superconductor. The benefit of having superconducting magnets is that the increased magnetic fields possible when high currents can be run through thin wires without fear of damage related to excessive resistive heating.

3.2 Luminosity

Luminosity is a one of parameter which shows the intensity of beam collisions. The higher the luminosity, the greater the chance of proton-antiproton collisions. The luminosity can be expressed as :

$$\mathscr{L} = \frac{f N_B N_p N_{\bar{p}}}{2\pi(\sigma_p^2 + \sigma_{\bar{p}}^2)} F(\frac{\sigma_l}{\beta^*}) \tag{3.1}$$

where f is the revolution frequency, N_B is the number of bunches, $N_{p(\bar{p})}$ is the number of protons(antiprotons) per bunch, and $\sigma_{p(\bar{p})}$ is the protons(antiprotons) RMS beam size

Parameter	Ran II
Number of bunch (N_B)	36
Bunch length [m]	0.37
Bunch spacing [ns]	396
Protons/bunch (N_p)	2.7×10^{11}
Antiprotons/bunch ($N_{\bar{p}}$)	3.0×10^{10}
Total antiprotons	1.1×10^{12}
β^* [cm]	35
Interactions/crossing	2.3

Table 3.1: Acclerator parameters for Run II configurations.

at the interaction point. F is a form factor which corrects for the bunch shape depends on the ratio between σ_l and the bunch length to the beta function β^* at the interaction point. The beta function that is a measure of the beam width is proportional to the beam's x and y extent in phase space. Table 3.1 shows the accelerator parameter in the Tevatron rnu(RanII). The peak luminosity is $\sim 4.4 \times 10^{32}\ cm^{-2}s^{-1}$. The delivered luminosity is 1.2 fb^{-1} and actual recorded luminosity is 1.0 fb^{-1}, which collected between February 2002 and September 2011. Figure 3.2 shows initial instantaneous luminosity and integrated luminosity measured with CDF.

3.3 The Collider Detector at Fermilab

The CDFII detector is a general purpose solenoidal detector which combines prexision charged particle tracking with projective calorimetry and fine grained muon detection. Figure 3.3 and Figure 3.4 show a cut away view and elevation view of the CDFII detector for each. Tracking systems are made up Silicon Trackers, Central Outer Tracker(COT), and Superconducting Solenoid which to measure precise trajectories and momenta of charged particles and reconstruct vertices. The solenoid surround the Silicon Trackers and COT, has 1.5m in radius and 4.8m long, and generates a 1.4T magnetic field parallel to the beam axis. Calorimetry Systems measure the energy of particles, surround the solenoid. Muon Chambers detect the particles penetrating both Tracking Systems and Calorimetry Systems. Muons deposit small amount of ionization energy in the material because they act as minimally ionizing particles(MIP), that is, the penetrating particles are mostly muons.

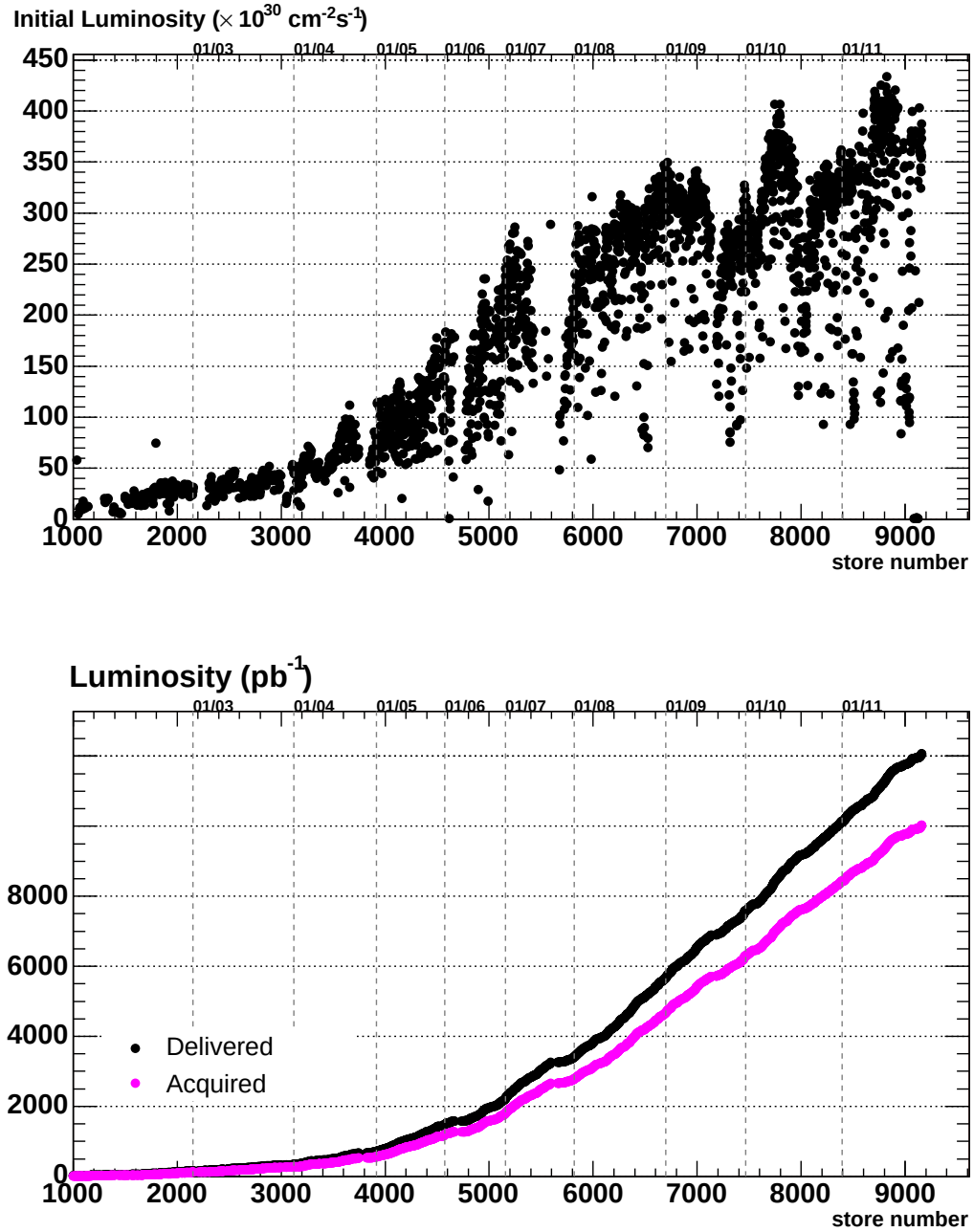

Figure 3.2: Initial instantaneous luminosity(top) and integrated luminosity(bottom) as a function of store number between February 2002 and September 2011.

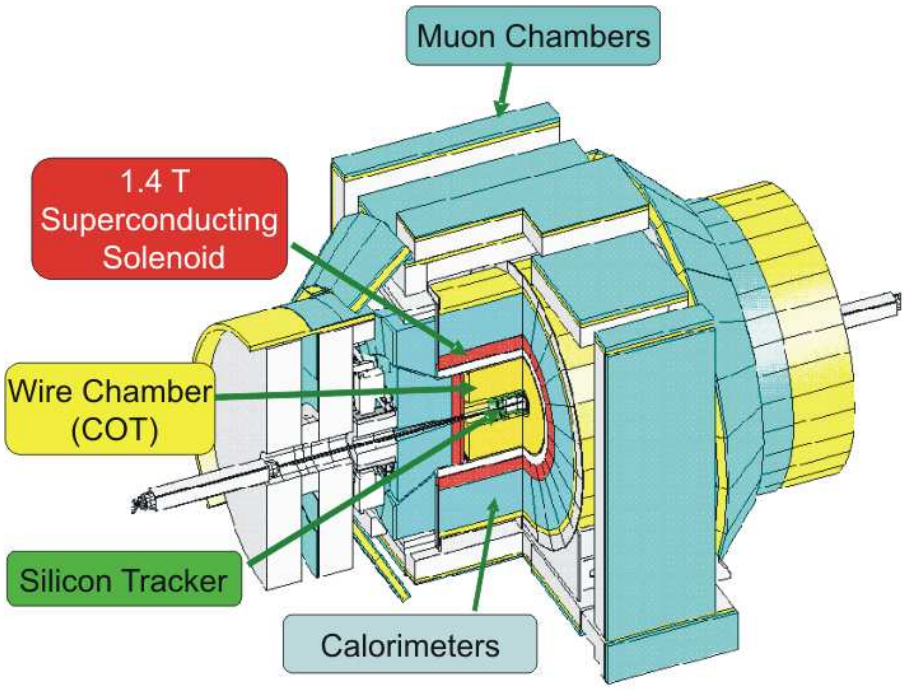

Figure 3.3: Cut away view of the CDF II detector.

3.3.1 Coordinate System in the CDF

In the CDF experint, the right-handed coordinate systems are used as standard coordinate system. Figure 3.5 shows the standard coordinate systems in the CDF. The z-axis is oriented the direction of the proton beam. The x-axis points horizontally away from the detector, and the y-axis is vertical pointing up-wards. It is helpful to use the cylindrical coordinate. The azimuthal angle ϕ is $x-y$ plane angle around the beam line. The polar angle θ is measured starting from the z-axis. The rapidity of a particle is defined as :

$$y \equiv \frac{1}{2}\ln(\frac{E + p_z}{E - p_z}) \tag{3.2}$$

where E is the energy of the particle and p_z is its longitudinal momentum. For highly boosted particles, $E \sim p$ and $p_z = p\cos\theta$, the rapidity can be approximated by pseudo-rapidity, which is defined as :

$$\eta = -\ln(\tan\frac{\theta}{2}). \tag{3.3}$$

In the CDF experiment, longitudinal direction(along the beam line) of momentum cannot be measured technically. Hence, the transverse components are used as kinematic imformations in analysis. When p is the magnitude of the momentum, the transverse momentum p_T is defined as follows.

$$p_T = p\,\sin\theta \tag{3.4}$$

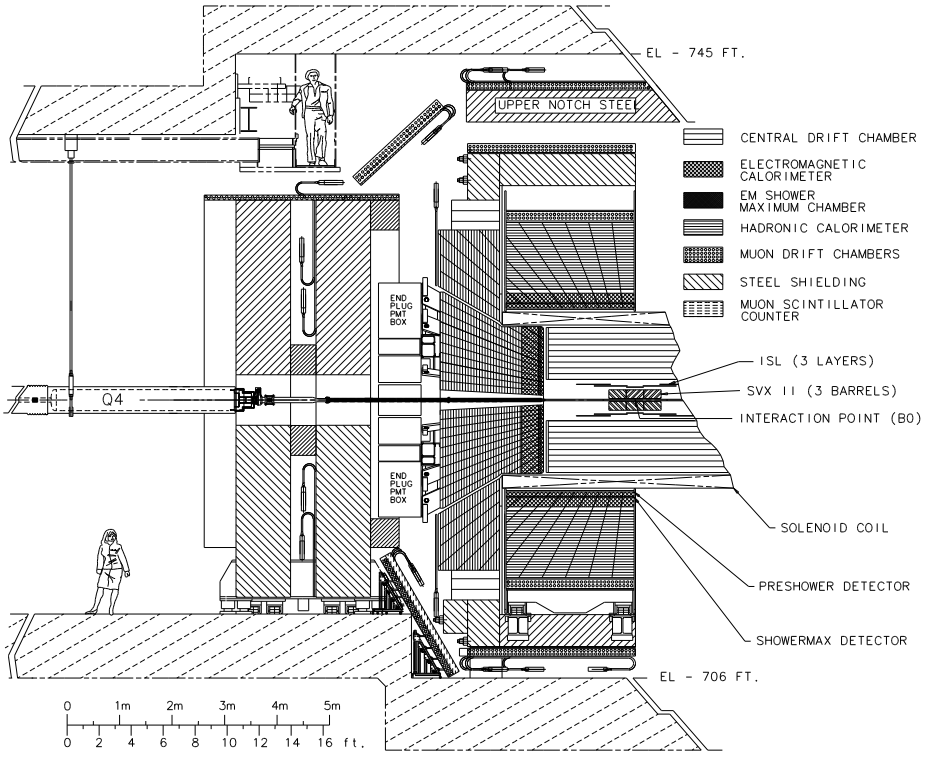

Figure 3.4: Elevation view of the CDF II detector.

3.4 Tracking Systems

For CDF analysis technique, precision charged particle tracking is very important. CDF II detector has an open cell drift chamber, the Central Outer Tracker(COT) covers the region $|\eta| \leq 1.0$. Inside the COT, a silicon "inner tracker" is built from three ccomponents. Layer 00(L00) is mounted on the beam pipe, very close to the beam line. Its primary purpose is to improve the impact parameter resolution. A micro-vertex detector at very small radii, so-called Silicon Vertex Detector(SVX-II), establishes the ultimate impact parameter resolution. Two additional silicon layers at intermediate radii, so called Intermediate Silicon Layers(ISL), provides p_T resolution and b-tagging in the forward region $1.0 \leq |\eta| \leq 2.0$, and stand-alone silicon tracking over the full region $|\eta| \leq 2.0$. The stand-alone silicon segments allow integrated tracking algorithms which maximize tracking performance over the whole region $\eta \leq 2.0$. In the central region ($\eta \leq 1.0$), the stand-alone silicon segment can be linked to the fill COT track to give excellent p_T and impact parameter resolution.

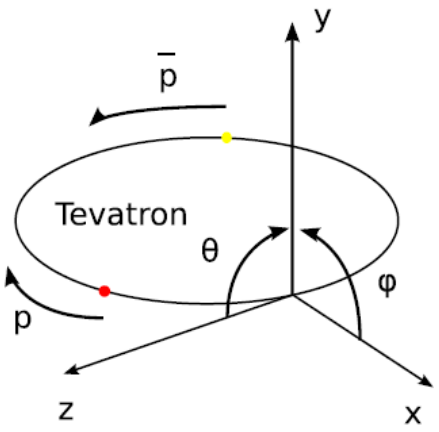

Figure 3.5: The standard coordinate system in the CDF.

3.4.1 Layer 00

Layer 00 is installed directly in the beam pipe. L00 was added at beginning of RunII for two reasons. Placement of a minimal material silicon layer at a smaller radius provides a precise measurement. Secondly, L00 was installed to extend the useful lifetime of the silicon system. The inner layers SVX-II will have a limited lifetime due to radiation damage. The design has six narrow(128 channels) and six wide(256 channels) groups in θ at $r = 1.35$cm and $r = 1.62$cm respectively. There are six readout modules in z, with two sensors bounded together in each module for a total length of 95cm. The sensors are single-sided p-in-n silicon with a 25(50)μm implant(readout) pitch. These have been produced by Hamamatsu Photonics(HPK), SGS-Tompson(ST) and Micron. These sensors can be biased up to 500V, limited by the maximum range of the power supplies.

3.4.2 Silicon Vertex Detector

Silicon Vertex Detector(SVX, SVX-II) is the core detector for silicon tracking and for a trigger on tracks with large impact parameter wit respect to the interaction point. The SVX-II detector has 5 layers of double-sided sensors surround the L00 at radii from 2.5 to 10.6cm. Three layers(L0, L1, and L3) are made of Hamamatsu silicon with the n strips perpendicular to the p strips. The remaining two layers(L2 and L4) are Micron sensors with a stereo angle of 1.2° between the n and p strips. The strip pitch varies between 60 to 140μm, depending on the layer radius. The maximum bias voltages that can be applied to Hamamatsu and Micron sensors are 170V and 70V respectively, limited by the breakdown voltage of the integrated coupling capacitors and subtle sensor effects. The SVX-II can provide track information to $|\eta| < 2.0$. Table 3.2 shows the design parameters of the SVX-II. Figure 3.7 shows 3D view and $r - \phi$ view for SVX-II.

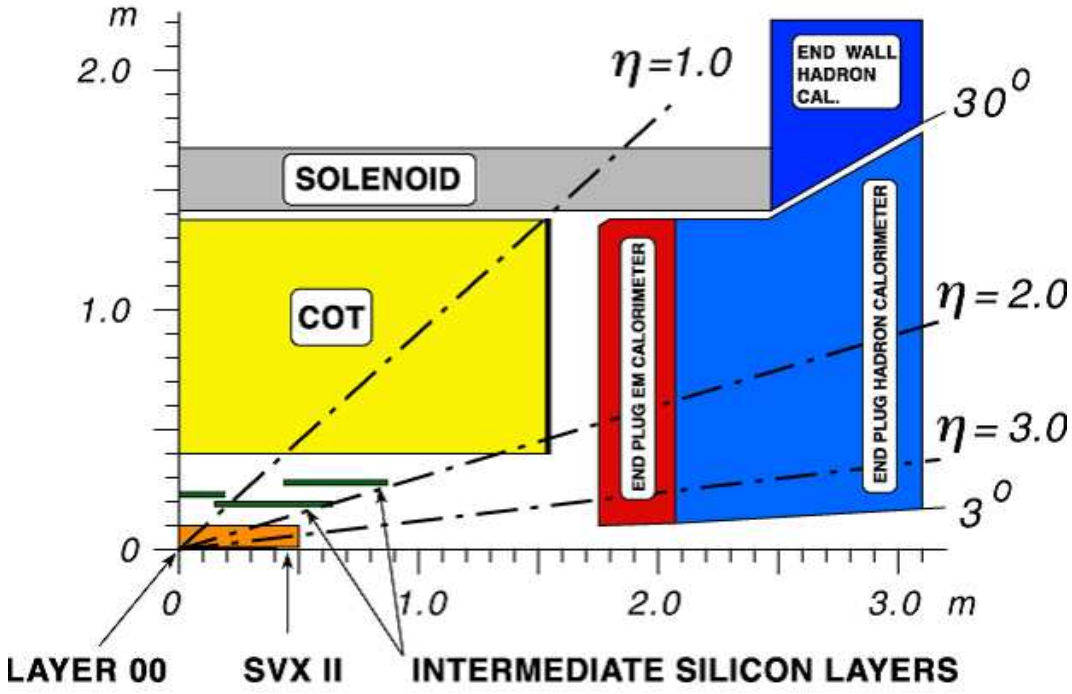

Figure 3.6: Longitudinal view of the CDF II tracking volume and plug calorimeter.

Parameter	**Layer 0 (L0)**	**Layer 1 (L1)**	**Layer 2 (L2)**	**Layer 3 (L3)**	**Layer 4 (L4)**
Number of ϕ strips	256	384	640	768	896
Number of z strips	512	576	640	512	896
stereo angle (degree)	90	90	+1.2	90	−1.2
ϕ strip pitch [μm]	60	62	60	60	65
z strip pitch [μm]	141	125.5	60	141	65
Total width [mm]	171.140	25.594	40.300	47.860	60.170
Total length [mm]	74.3	74.3	74.3	74.3	74.3
Active width [mm]	15.300	23.746	38.340	46.020	58.175
Active length [mm]	72.43	72.43	72.38	72.43	72.38
Number of sensors	144	144	144	144	144

Table 3.2: Design parameters of the Silicon Vertex Detector.

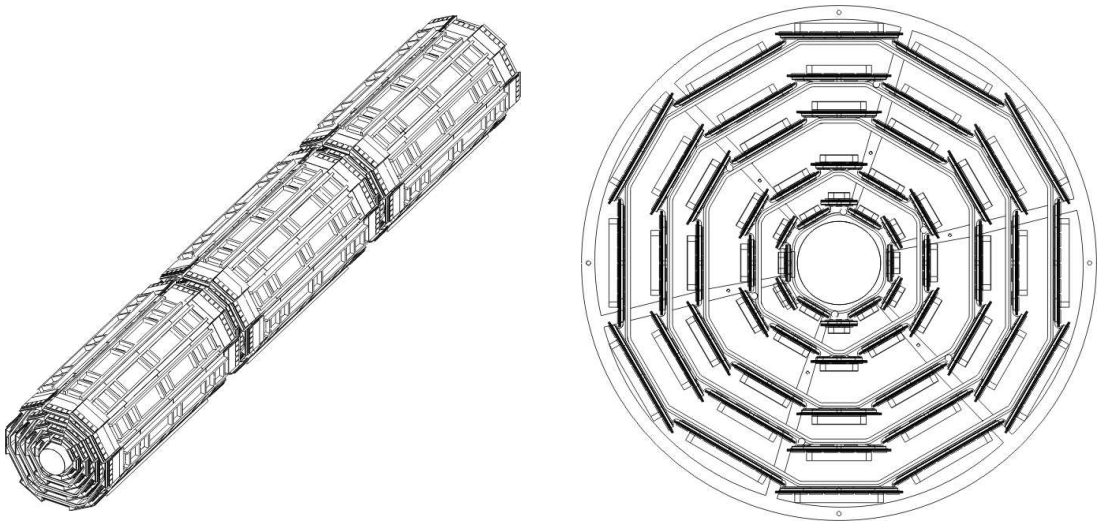

Figure 3.7: 3D view of the three barrels(left) and $r-\phi$ view of the barrel showing the 12 wedges with the 5 layers(right).

3.4.3 Intermediate Silicon Layer

Intermediate Silicon Layers(ISL) provides an extended forward coverage and links tracks between the COT and the SVX-II and also can provide stand-alone 3D track information in the forward region. Figure 3.8 shows the 3D view of the ISL spaceframe. The ISL detector has one central layer at radius of 22cm covering $|\eta| < 1.0$, and two forward layers at radii of 22cm and 28cm covering $1 < |\eta| < 2$, with total length of 3m. It is made of double-sided silicon with strips at a stereo angle of 1.2°, and a strip of 112μm. The breakdown voltage of the sensors is 100V limited by the breakdown voltage of the coupling capacitors. Figure 3.9 shows the $r-\phi$ and $r-z$ views of the silicon detectors.

3.4.4 Central Outer Tracker

The Central Outer Tracke(COT) is a cylindrical open-cell drift chamber spanning from 44 to 132cm in radii, and 310cm long. It operates inside a 1.4T solenoidal magnetic field and is designed to find charged tracks in the region $|\eta| \leq 1.0$. The hit position resolution is approximately 140μm and the momentum resolution $\sigma(p_T) = 0.0015(GeV/c)^{-1}$. The COT is segmented into 8 super-layers alternating stereo and axial, with a stereo angle of ±2°. Each super-layer contains 12 sense wires alternated with 13 potential wires which provide the field shaping within the cell yielding a total of 96 measurement layers. For the entire cell chamber, there are 30,240 sense wires and 32,760 potential wires. Operating

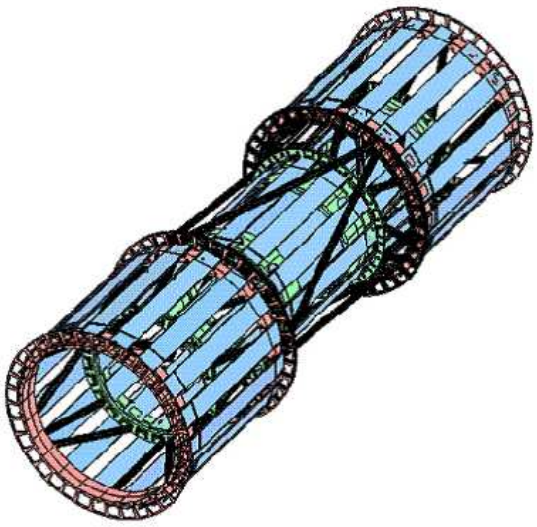

Figure 3.8: 3D view of the ISL spaceframe.

with an Argon-Ethane(50:50) gas mixture the maximum drift time is approximately 180ns. The cells are tilted at 35° to account for the Lorentz angle such that the drift direction is azimuthal. Tracks originating from the interaction point which have $|\eta| < 1$ pass through all 8 superlayers of the COT. Tracks which have $|\eta| < 1.3$ pass through 4 or more superlayers. Table 3.3 shows a mechanical summary of the COT. Figure 3.10 shows cell layout for super-layer-2(SL2). Figure **??** shows the east endplate slots sense and field planes.

3.5 Calorimeter Systems

Segmented electromagnetic and hadron sampling calorimeters surround the tracking system and measure the energy flow of interacting particles in the $|\eta| < 3.6$. Thecalorimeter systems are divided into 2 systems with respect to the pseudo-rapidity range, central and plug(forward) region. The Central Electromagnetic Calorimeter(CEM) covers the $|\eta| < 1.1$ region, which uses lead sheets interspersed with polystyrene scintillator as the active medium and employs phototube readout. The Central Hadronic Calorimeter(CHA) covers the $|\eta| < 0.9$ region, which uses steel absorber interspersed with acrylic scintillator as the active medium. The plug calorimeters, Plug Electromagnetic Calorimeter(PEA) and Plug Hadron Calorimeter(PHA), cover the $1.1 < |\eta| < 3.6$ region. They are sampling scintillator calorimeters which are read out with plastic fibers and phototubes.

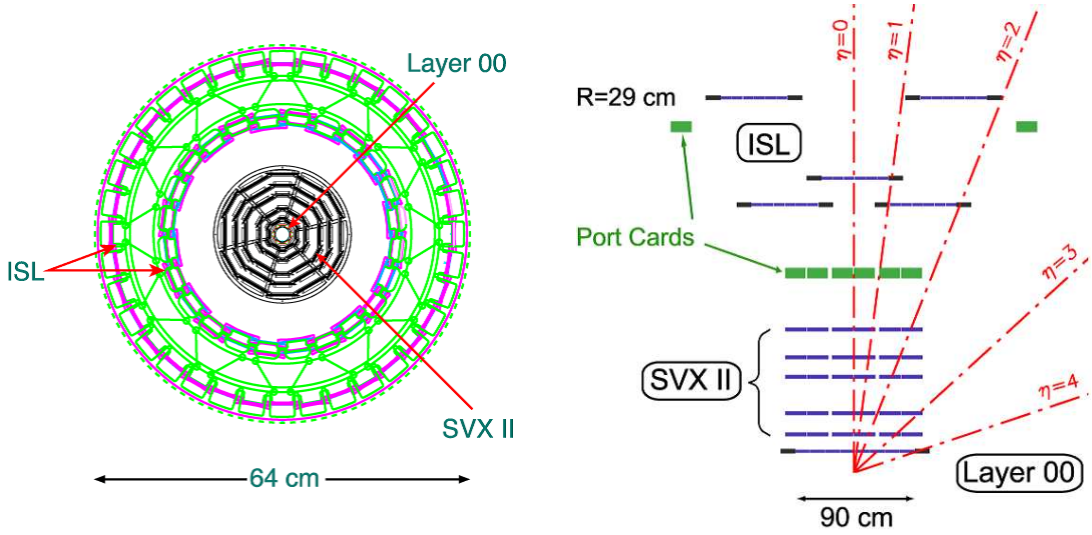

Figure 3.9: $r-\phi$ view(left) and $r-z$ view(right) of the silicon detector.

3.5.1 Central Calorimeter

The Central Electromagnetic Calorimeter detects electrons and photons and measure their energy. It is a lead-scintillator sampling system with tower segmentation, the each tower is 15° in $r-\phi$ plane. The CEM total thickness is 18 radiation length(32cm), to make sure that 99.7% of the electrons energy will be deposited. The CEM energy is

$$\frac{\sigma_E}{E} = \frac{13.5\%}{\sqrt{E_T}} \oplus 2\% \tag{3.5}$$

where E_T is the transverse energy in GeV, $\oplus$ symbol means that the constant term is added in quadrature to the resolution, and position resolution is typically 2mm for 50GeV/c electrons.

The Central Electromagnetic Showermax Chamber(CES) is used to identify electrons and photons using the position measurement to match with tracks, the transverse shower profile to separate photon from $\pi^0 s$, and pulse hight to help identify electromagnetic showers. The CES is located at approximately 6 radiation lengths deep at the expected shower maximum of particles in the EM calorimeter. The CES module is a multi-wire proportional chamber with 64 anode wires parallel to the beam axis.

The Central Preshower Detector(CPR) is located at between the front face of the EM calorimeter and the magnet coil. The CPR can be useful in π-photon separation and electron identification. The CPR was replaced the slow gas chamber with a faster scintillator version which has a better segmentation during RunII in 2004. The new CPR is used to improve the jet energy resolution.

The Central Hadronic Calorimeter is an iron-scintillator sampling calorimeter, covering range $|\eta| < 0.9$, approximately 4.5 λ_0 interaction length, and the energy resolution

Parameter	
Gas (Argon:Ethane)	(50:50)
Number of Layers	96
Number of Super-layers	8
Stereo Angle (degree)	+2, 0, -2, 0, +2, 0, -2, 0
Cells/Layers	168, 192, 240, 288, 336, 384, 432, 480
Sense Wires/Cell	12, 12, 12, 12, 12, 12, 12, 12
Radius at Center of SL (cm)	46, 58, 70, 82, 94, 106, 117, 129
Tilt Angle	35°
Material Thickness	1.6% X_0
Drift Field	1.9 kV/cm
Maximum Drift Distance	0.88 cm
Maximum Drift Time	177 ns
Number of Channels	30, 240

Table 3.3: Design parameters of the Central Outer Tracker.

is

$$\frac{\sigma_E}{E} = \frac{50.0\%}{\sqrt{E_T}} \oplus 3\%. \tag{3.6}$$

The Wall Hadronic Calorimeter(WHA) also an iron-scintillator sampling calorimeter, covering range $0.7 < |\eta| < 1.3$. The WHA is 4.5 λ_0 interaction length, and the energy resolution is

$$\frac{\sigma_E}{E} = \frac{75.0\%}{\sqrt{E_T}} \oplus 4\%. \tag{3.7}$$

3.5.2 Plug Calorimeter

The plug calorimeter covers $1.1 < |\eta| < 3.6$, corresponding to polar angles $3° < \theta < 37°$ as shown in Figure **??**. Each plug wedge spans 15° in azimuth, however from $1.1 < |\eta| < 2.1$ (37° to 14°) the segmentation in ϕ is doubled, and each tower spans only 7.5°. There is an electromagnetic section(PEM) with a shower position detector(PES), followed by a hadronic section(PHA).

The PEM is lead-scintillator sampling calorimeter, with unit layers composed of 4.5mm lead and 4.0mm scintillator. There are 23 layers in depth for a total thickness of about 21 X_0 radiation length at normal incidence. The PEM has an energy resolution is

$$\frac{\sigma_E}{E} = \frac{16\%}{\sqrt{E_T}} \oplus 1\%. \tag{3.8}$$

The PHA is an iron-scintillator sampling calorimeter, approximately 7 λ_0 in depth, and has an energy resolution of

$$\frac{\sigma_E}{E} = \frac{80\%}{\sqrt{E_T}} \oplus 5\%. \tag{3.9}$$

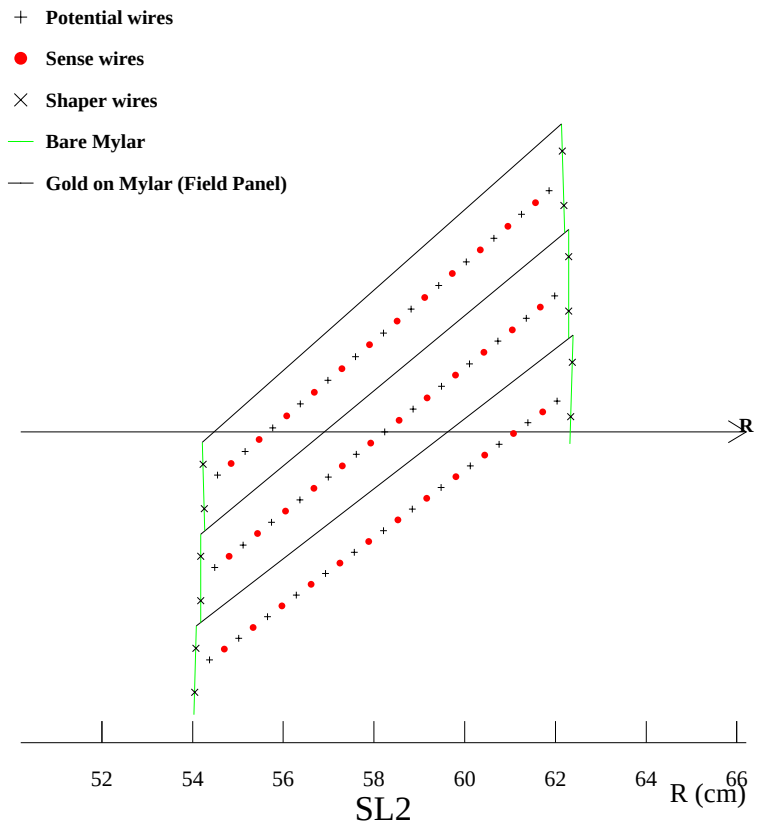

Figure 3.10: Nominal cell layout for SL2.

The PEM shower maximum detector is located about 6 λ_0 deep within the PEM, and is constructed of two layers of scintillating strips. The strips are 5mm wide, and roughly square in cross section. Position resolution of the PES is about 1mm. The summaries of design parameters for the calorimeter are shown in Table 3.4.

3.6 Muon Detectors

Muons penetrate the tracking systems and the calorimeters leaving very little energy. The reason is muons produce much less bremsstrahlung than electrons and therefore do not produce electromagnetic showers, due to their larger mass. The CDF muon systems use this property by placing detectors behind enough material. Muon deposit minimum ionizing energy in the calorimeters matched with a track in the COT. The momentum of these muons is measured by their bend in the solenoidal field using the COT. The central muon system is capable of detecting with transverse momentum $p_T \geq 1.4$GeV,

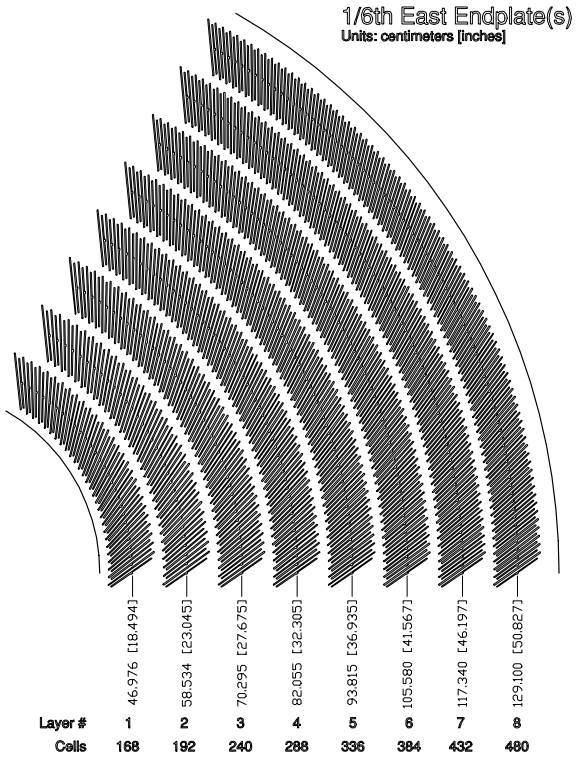

Figure 3.11: East endplate slots sense and field planes are at the clock-wise edge of each slot.

through their interaction with the gas and subsequent drift on the produced electrons toward the anode wires. The muon detectors consist of four separate subsystems:

- The Central Muon Chambers(CMU)
- The Central Upgrade(CMP)
- The Central Muon Extension(CMX)
- The Barrel Muon Detector(BMU)

Table 3.5 shows design parameters of muon detector. Figure 3.13 shows the effective muon detector coverage in $\eta - \phi$ plane.

The CMU detector located directly outside of the central hadron calorimeter, 35m from the interaction point, and covers the region of $|\eta| \leq 0.6$. It is divided into 24 east and 24 west 15° wedges. Each wedge contains three muon chambers and each muon chamber consists of four layers of four rectangular drift cells staggered in order to eliminate hit position ambiguities. A stainless steel sense wire a diameter of 50μm is located in the center of each cell. A muon object is created by forming a "stub" from hits in the muon chambers matching it to extrapolated COT tracks.

The CMP consists of second set of muon chambers behind additional 60cm of steel in the region $55° \leq \phi \leq 90°$. The chambers are fixed length in z and from box around

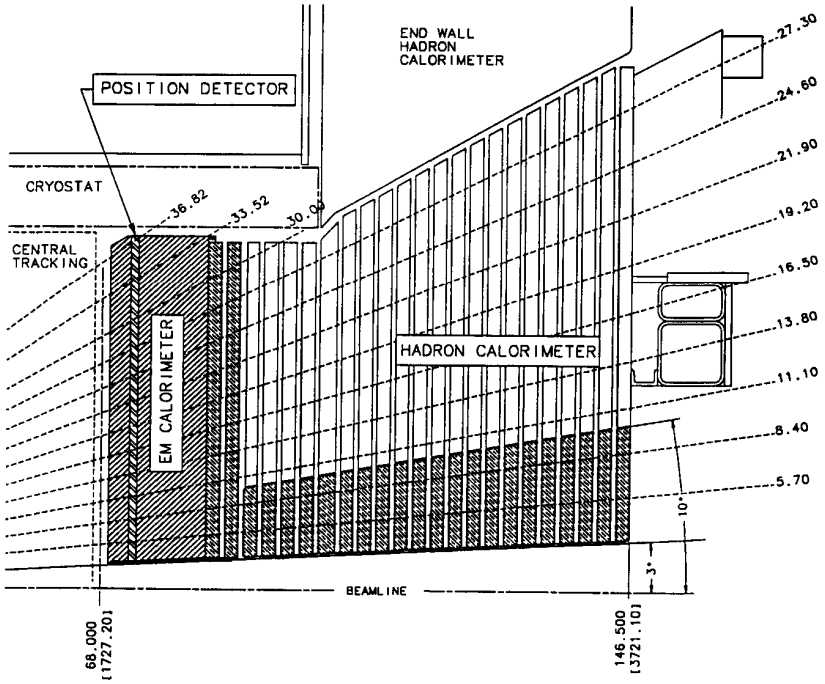

Figure 3.12: Cross section of the plug calorimeter(PEM and PHA).

the central detector. The pseudorapidity coverage thus varies with azimuth as shown in Figure 3.13.

The central extension consist of conical section of drift tubes(CMX) in polar angle from 42° to 55°($0.6 \leq |\eta| \leq 1.0$). The top two wedges(Wedge 5 and 6) of the west CMX is called the "Keystone". There are no top two wedges on the east CMX due to cryogenic utilities servicing the solenoid. The bottom 6 wedges(Wedge 15-20) are called "Miniskirt". Figure 3.14 shows the CMX detector in $r - \phi$ plane.

Calorimeter	**Coverage**	**Energy Resolution (%)**	**Thickness**	**Absorber**
CEM	$\eta < 1.1$	$13.5/\sqrt{E_T} \oplus 2$	18 X_0	3.18mm lead
PEM	$1.1 < \|\eta\| < 3.6$	$16.0/\sqrt{E_T} \oplus 1$	21 X_0	4.5mm lead
CHA	$\|\eta\| < 0.9$	$50.0/\sqrt{E_T} \oplus 3$	4.5 λ	2.5cm iron
WHA	$0.7 < \|\eta\| < 1.3$	$75.0/\sqrt{E_T} \oplus 4$	4.5 λ	5.0cm iron
PHA	$1.3 < \|\eta\| < 3.6$	$80.0/\sqrt{E_T} \oplus 5$	7.0 λ	5.08cm iron

Table 3.4: Design parameters of the calorimeter.

Muon detector	**CMU**	**CMP**	**CMX**
Coverage	$\|\eta\| < 0.6$	$\|\eta\| < 0.6$	$0.6 < \|\eta\| < 1.0$
Drift tube length [cm]	226	640	180
Max drift time [μs]	0.8	1.4	1.4
Total drift tubes	2304	1076	2208
Pion interaction length (λ)	5.5	7.8	6.2
Minimum detectable muon p_T (GeV/c)	1.4	2.2	1.4

Table 3.5: Design parameters of the muon detector.

3.7 Luminosity Monitor

The beam luminosity has been measured using the process of inelastic $p\bar{p}$ scattering. The cross section is $\sigma_{in} \sim 60$mb. The rate of inelastic $p\bar{p}$ interaction is given by

$$\mu f_{\rm BC} = \sigma_{\rm in} L \tag{3.10}$$

where L is the instantaneous luminosity, $f_{\rm BC}$ is the rate of bunch crossing in the Tevatron and μ is the average number of $p\bar{p}$ interaction per bunch crossing. In CDF RunII, Cherenkov luminosity counters(CLC) is used to meacure the luminosity by counting number of $p\bar{p}$ interaction μ accurately.

The detector consists of two modules which are located in the "3 degree holes" inside the end-plug calorimeter in the forward and backward region and which cover $3.7 < |\eta| < 4.7$ range. Each CLC detector module consists of 48 thin, long, conical, gas-filled Cherenkov counters. The counters arranged around the beam pipe in three concentric layers, with 16 counters each, and pointing to the center of the interaction region. They are built with reflective aluminized mylar sheets of 0.1mm thick and have a conical shape. The cones in two outer layers are about 180cm long and the inner layer counters have the length of 110cm. The Cherenkov light is detected with fast, 2.5cm diameter, photomultiplire tubes. The tubes have a concave-convex, 1mm thick, quartz window for efficient collection of the ultra-violet part of Cherenkov spectra and operate at a gain of 2×10^5. The counters are mounted inside a thin pressure wessel made of aluminun and filled with isobuthan. The systematic uncertainty of the luminosity measurement is dominantly coming from the uncertainty of the inelastic $p\bar{p}$ cross section($\sim$3%), the CLC acceptance($\sim$2%, and the non-lineality of the CLC acceptance due to CLC occupancy saturates as growing luminosity due to the finite number of counters($< 2\%$).

3.8 Trigger Systems

The trigger plays an important role on hadron collider experiment because the collision rate is much higher than the rate as which data can be stored on tape. The crossing

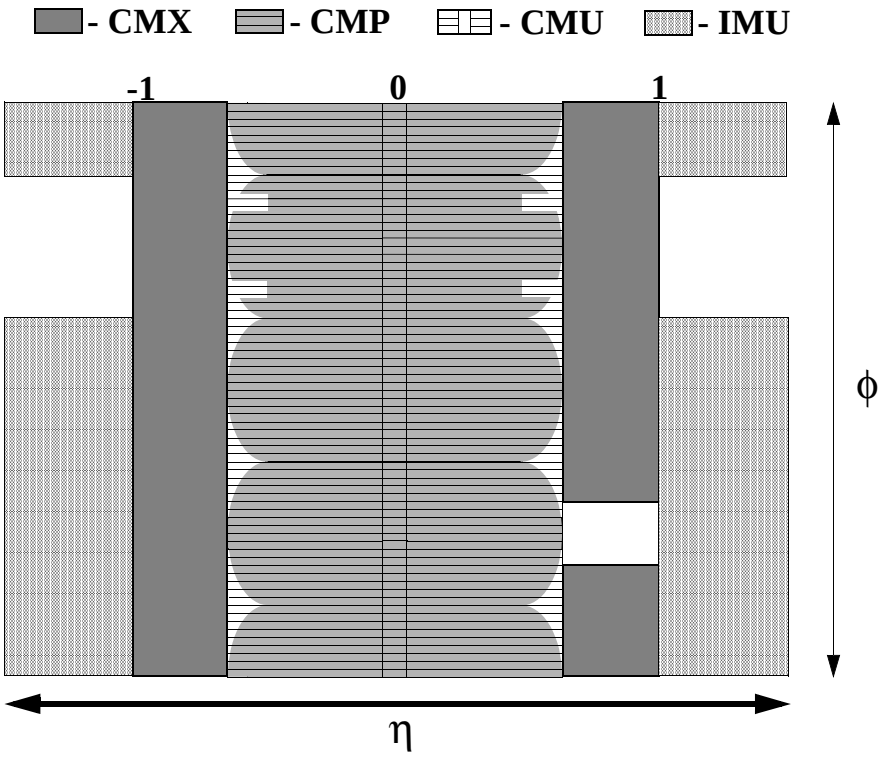

Figure 3.13: Muon detector coverage in $\eta - \phi$ plane.

rate of the Tevatron under 36 on 36 bunch operation is 7.6MHz, corresponding to 396ns collision separation. The role of the trigger is to effectively extract the most interesting physics events from the large number of minimum bias events. For RunII, CDF employs a three-level trigger system to selectively capture interesting events. The levels are denoted simply as "L1", "L2" and "L3", with each subsequent level making more complicated decisions and requiring successively longer processing times. Figure 3.15 shows schematic of the CDF trigger system.

3.8.1 Level-1

The first level of trigger selection Level-1(L1) uses custom designed hardware to find physics objects based on a subset of the detector information and then makes a decision based on simple counting of these objects. The input to the L1 hardware comes from the calorimeters, tracking chambers and muon detectors. The decision to retain an event for further processing is based on the number and energies of the electron, jet and muon candidates as well as the missing energy in the event, or on the kinematic properties of these objects. The L1 hardware consists of three parallel synchronous processing streams which feed inputs of the single Global L1 decision unit. One stream finds calorimeter

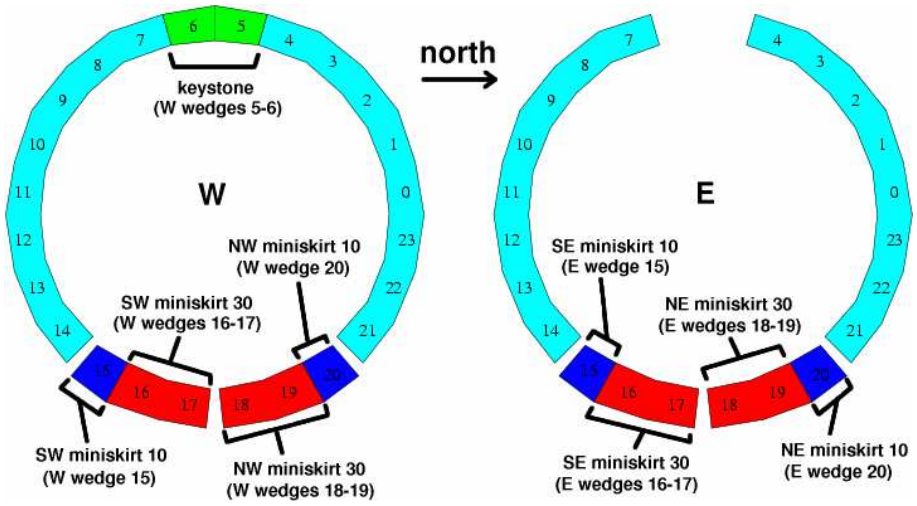

Figure 3.14: CMX detector in $r - \phi$ plane.

objects, another finds muons and third finds tracks in the central region. The L1 trigger can be formed using these streams singularly as well as AND or OR combinations of them. All elements of the L1 trigger are synchronized to the same 132ns clock, with a decision made every 132ns by Global L1. In the period of the data taking considered in this analysis the accelerator was the two intermediate clock cycles automatically rejected. The maximum L1 accept rate is 20kHz, while the typical one is 12kHz.

3.8.2 Level-2

Events accepted by L1 are processed by the second level of trigger Level-2(L2), which is composed of several asynchronous subsystems. These provide input data to programmable L2 processors on the Grobal L2 crate, which determine if any of the L2 trigger are satisfied. Processing for L2 trigger decision starts after the event written into one of the four L2 buffers by a L1 accept. When L2 is analyzing the event in one of buffers, that buffer cannot be used additional L1 accept. If all the four are full, the deadtime of the data acquisition is increased. It follows that the time required for a L2 decision needs to be less than about 80% of the average time between L1 accepts in order to keep the deadtime as low as possible. For this purpose L2 has been pipelined into two stages each taking approximately 10μs, which is sufficient to keep the deadtime at a minimum, even if L1 had an accept-rate of 50kHz. The L2 buffers perform a limited event reconstruction using essentially all the information used in L1, but with higher precision. In addition, at L2, data from the central shower-max detector and the SVX are available, which improve respectively the identification of electrons and photons and the reconstruction of the secondary vertices. Furthermore, a jet reconstruction algorithm is provided by the L2 cluster finder. After all of the data are stored in the processors, the event is examined to check if the criteria of any of the L2 triggers have

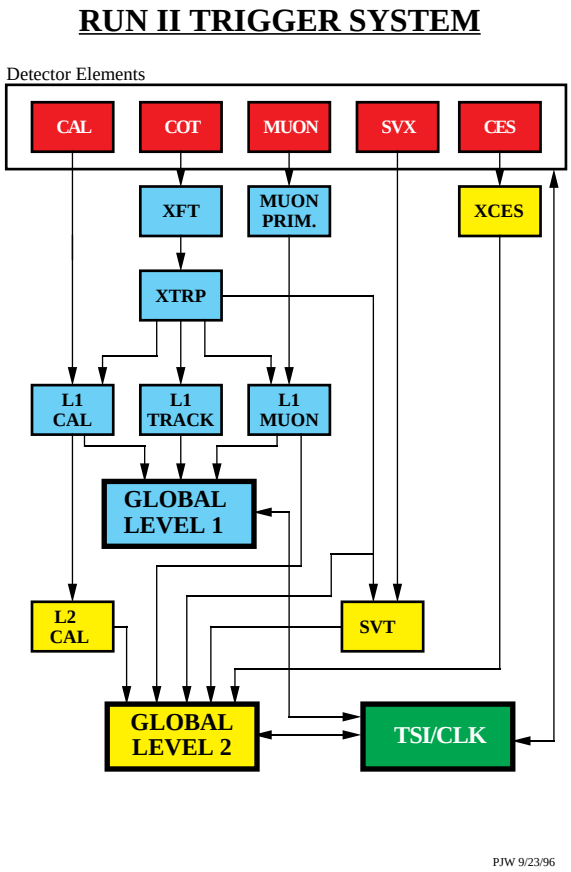

Figure 3.15: Book diagram of the trigger pass for Level-1 and Level-2.

been satisfied. This operation can be performed while the new events are being loaded into memory, thus not affecting the deadtime. The typical L2 accept rate, as of this writing, is between 100 and 300Hz, depending on the initial luminosity.

3.8.3 Level-3

The Level-3(L3) trigger subsystem is composed of two main components, the Event Builder(EVB) and the L3 Farm. L1 and L2 systems need to make their decisions at very high rate which makes it impossible to fully reconstruct each event. While L1 and L2 algorithms use small predefined pieces of event data to make their decision, the event pieces are stored in the buffers of the 140 Front End crates which constitute the EVB. After a L2 decision is made, the Event Builder assembles all event fragments from the Front End crates into one data block.

The 16 subfarms which compose the L3 Farm recieve event fragments from the EVB and build complete events into the appropriate data structure for analysis. Since it takesabout one second for one computer unit to make a trigger decision on one event, it

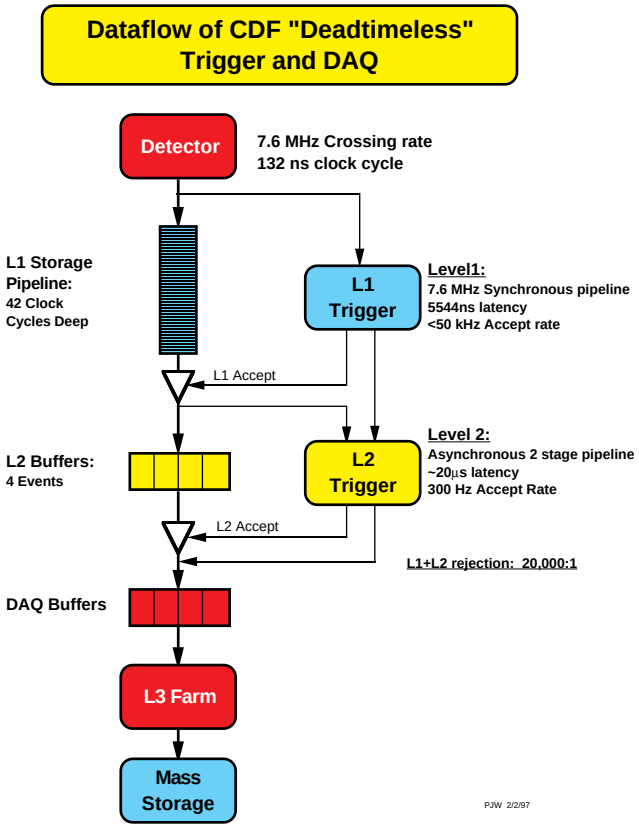

Figure 3.16: Schamatic diagram of the trigger and DAQ.

takes a large farm of 250 Dual Pentiun Linux personal 5 computers(called "processors") to ensure the required input rate. Each subfarm contains between 14 and 18 processor nodes and one "converter" node, which acts as "farm input" distributing the data flow coming from the EVB.

The events are then passed to a trigger algorithm(a different one for each processor) that categorizes the event and makes the decision as to whether or not to permanently store it. The selected event are passed to the Data Logger subsystem. During the building processing, the event integrity is checked. The L3 algorithms take advantage of the full detector information and improved resolution unavailable to lower trigger levels. This includes full three-dimensional track reconstruction and tight matching of tracks to calorimetor and muon-system imformation. Results from the lower level are used or drive the algorithms, which are based on the off-line analysis packages. Thisis a modular and separated filter modules for specific triggers. L3 accept events with a rate of approximately 75Hz.

Chapter4

Event Selection

Physics objective in this study is to search for the chargino-neutralino pare production using high-p_T like-sign dilepton events($ee,\ e\mu,\ \mu\mu$), such event occurs in the following process,

$$qq' \to \tilde{\chi}_1^{\pm}\tilde{\chi}_2^0 \to \ell^{\pm}\ell^{\pm}\ +\ X. \tag{4.1}$$

The desirable events are collected by using trigger systems as described in previous chapter and series of lepton selection criteria in efficiently.

First, the trigger system collects the events roughly, however removes the undesirable events, i.e. background events, for example the event coming from inelastic $p\bar{p}$ collisions.

In second step, the event collected by trigger system are imposed the series of lepton selection criteria to reject the backgrounds as possible. The selection criteria are constructed by taken the lepton properties and the detextor response for the leptons into account.

4.1 Dataset and Triggers

To collect the events efficiently, the data collected by inclusive high-p_T lepton(electron and muon) trigger is used.

The inclusive high-p_T electron trigger requires at least a electron satisfied the series of electron selection and some large E_T requirement. Some concretely speaking, the trigger selects the events have a object which deposit its some large energy to electromagnetic calorimeter($E_T > 18$GeV) and the energy deposition ratio(HAD/EM) is less than 0.124 and lateral shower profile(L_{shr}), and the position matching on z derection between CES and extrapolated track($\Delta_{z_{CES}} < 8$cm). The criteria is applied to events in step by step, i.e. Level-1, Level-2, and Level-3, to reduce the data taking rate due to the capability limit for the trigger system. The trigger criteria are changed in tun by run due to the performance and condition of CDF detector and Tevatron accelerator.

The inclusive high-p_T muon trigger requires at least a muon satisfied the series of muon selection and some large p_T requirement. The muon trigger are mainly categorized into CMUP muon trigger and CMX muon trigger, CMUP muon means a track object points to both CMU and CMP detector, while CMX muon points to CMX detector. The CMUP muon trigger requires CMUP muon with XFT track $p_T > 18$GeV/c and the position matching in x direction between the position on muon detectors, both CMU and CMP, and track. And the CMX muon trigger requires CMX muon with $p_T > 18$GeV/c and the position matching same as CMUP muon trigger.

4.2 Event Selection

As described before, the desirable events are high-p_T LS dilepton events to search for the chargino-neutralino pair production. CDFII has well-defined algorithm to identify electrons or muons by using track reconstruction, energy clustering, and other particle proper reaction to detectors. The particle identifications are not used to effectively picking up desirable events, but reduce the background such as fake lepton. To further pick up the good events, there are more event selection criteria, as mentioned after sections.

4.2.1 Pre-Event Selection

The Pre-Event Selections are first used in several studies and estimations described in this thesis, for instance background estimations. One of them is used to ensure well-defined measurement of collisions with detector. The selection requires the vertex with the highest p_T-sum of associated tracks, so-called "primary vertex", within the region in z plane, i.e. $|z_{pv}| < 60$cm.

The Cosmic ray veto is also required as the Pre-Event Selection. The cosmic rays contaminate the physics event, coming from collision, by mimicking muons or electrons. While the cosmic rays are coming from outside of the detector, the muon with collisions are coming from center of detector. And the Cosmic rays cross the detector at any time with respect to the beam crossing. The cosmic ray veto is achieved to look at the direction of the trajectory and crossing timing.

4.2.2 Lepton Identification

The Electron Identification is achieved by using series of selection criteria, tracking and energy clustering validated using test beam. Central electron(CEM), Central muon(CMUP and CMX) are only desirable object in the thesis, i.e. $|\eta| < 1.2$. The selections are categorized into 3 parts, "geometrical and kinematics cuts", "track quality cuts", and "identification cuts(ID cuts)".

Geometrical and kinematical cuts

- Electron Fiducial :

  This variable ensures that the electron is reconstructed in a region of the detector which well instrumented. The electron position in the CEM is determined using either the value determined by the CES shower or by the extrapolated track, and it must satisfy the following requirements.

  - The electron must lie within 21cm of the tower center in the $r - \phi$ view in order for the shower to be fully contained in the active region $|z_{CES}| < 21$cm.

- The electron should not be in the regions $|z_{CES}| < 9$cm, where the two halves of the central calorimeter meet, and $|z_{CES}| > 230$cm, which corresponds to outer half of the last CEM tower. This region is prone to leaking into the hadronic part of the calorimeter.
- The electron should not be in the region immediately closest to the point penetration of the cryogenic connections to the solenoidal magnet, which is uninstrumented. This corresponds to $0.77 < \eta < 1.0$, $75 < \phi < 90$ degree, and $|z_{CES}| < 193$cm.

- Muon Fiducial :

  Muons are identified by matching hits in the muon chambers with a reconstructed track and energy in the calorimeter on the trajectory of the particle. The muons pass through the muon chambers, than the muon tracking is formed using the hit imformation and fitting algorithm(Muon (stub) reconstruction). The muon stub has at least three hits associated to it.

  - The fiducial distance of the tracks extrapolated to muon chambers in the $r-\phi$ plane and z-direction.
  - COT exit radius ρ :

    To ensure that CMX muon pass through all eight COT superlayers, CMX muons require COT exit radius ρ of the track. ρ is defined as,

    $$\rho = \frac{\eta}{|\eta|} \cdot \frac{z_{COT} - z_0}{\tan(\pi/2 - \theta)} \tag{4.2}$$

    where z_{COT} is used for the length of the COT(155cm).

- High transverse energy(E_T) :

  The transverse electromagnetic energy deposited by electron is calculated as the electromagnetic cluster energy multiplied by sinθ, where θ is the polar angle provided by the best COT track pointing to the EM cluster.

- High transverse momentum(p_T) :

  The transverse momentum of the COT track as measured by using the track curvature in the COT.

Track quality cuts

- COT hits requirement :

  To ensure that the track associated with the electron or muon is good quality reconstructed track, require that track has been reconstructed in the COT in 3 axial and 3 stereo superlayers with at least 7 hits in each.

- The relative position to primary vertex in z plane($z_0 - z_{pv}$) :

  Separation between z coordinate of the closest approach point with respect to run averaage beam lin(z_0) and primary vertex z position(z_{pv}).

- Silicon hits requirement :

  The track isrequired hitting to some SVX layers(> 3). The requirement critical plays to reject the residual photon conversion events which are considerable background in the LS dilepton events.

- Impact parameter(d_0) :

  This variable is recalculated to take the x coordinate of the primary vertex. The cuts is the most powerfully for rejecting cosmic rays background.

Isolation cut

- Isolation($\mathrm{ISO}_{0.4}^{cal}$) :

  The leptons are required to be isolated in terms of the calorimeter cone-isolation with cone size of $\Delta R = \sqrt{\Delta\eta^2 + \Delta\phi^2}$. The calorimeter isolation is defined for track objects. It is

$$\mathrm{ISO}_{0.4}^{cal} = \sum_{\Delta R<0.4} E_T^{(i)} - (E_T^{(seed)} + E_T^{(\eta+1)} + E_T^{(\eta-1)}) \tag{4.3}$$

  where $E_T^{(i)}$ is the tower E_T summed over the electromagnetic and hadronic calorimeter, $E_T^{(seed)}$ is the E_T of the tower that the track is pointing, and $E_T^{(\eta)\pm 1}$ is the same quantities for the towers in the same wedge but with the η index off by the 1 with respect to the seed tower.

Electron Identification cuts

- Ration of hadronic and electromagnetic energy(HAD/EM) :

  The ration should be small, that is, energy deposition in electromagnetic calorimeters is much higher than energy deposition in hadronic calorimeter.

- EM shower shape(L_{shr}) :

  The purpose of this quantity is to provide som discrimination of electrons and photons from hadronic showers faking these particles in the central electromagnetic calorimeter. This is done by comparing the observed the energy in CEM towers adjacent to seed tower to expected electromagnetic shower taken with test beam data.

$$L_{shr} = 0.14 \sum_i \frac{E_i^{adj} - E_i^{(exp)}}{\sqrt{(0.14\sqrt{E})^2 + (\Delta E_i^{(exp)})^2}}, \tag{4.4}$$

  where $E_i^{(adj)}$ is the measured energy in tower adjacent to the seed tower, $E_i^{(exp)}$ is the expected energy in the adjacent tower from test beam data, $\Delta E_i^{(exp)}$ is the error on the energy estimate.

- Ratio of the cluster energy to the momentum(E/p) :

  If a object pointing calorimeter cluster is electron, its momentum measured by COT track matches to the energy in the calorimeter cluster, i.e. $E/p \sim 1$.

- The pulse height shape in CES(χ^2_{strip}) :

  The pulse height shape in the CES detector in the $r-z$ view is compared to the test beam data using the χ^2 test.

- Track matching to CES cluster(Δz_{CES} and $Q \times \Delta x_{CES}$) :

  The extrapolated track is required to match a CES cluster in $r-\phi(x)$ and z plane. The $r-\phi$ plane requirement is asymmetry due to the trajectory of track in the detector. If the sign of charge and Δx is opposite, the track traverses a larger part of the calorimeter in adjacent towers, which results in more radiation and less precise position.

- Conversion removal :

  A photon traveling through material converts into an electron-positron pair. However the electron is true electron, it not directly comes from hard scattering events(prompt electron). To remove the conversion electron, conversion tagging algorithm is used. The algorithm requires to opposite charge of electrons the following,

  $$|\Delta\cot\theta| < 0.04, \text{ and } |\delta_{xy}| < 0.2, \tag{4.5}$$

  $\cot\theta$ is the difference between the polar angle cotangents of the tracks. δ_{xy} is the separation between the tracks in the $r-\phi$ plane.

Muon Identification cuts

- Small calorimeter deposition(EM and HAD) :

  Muons deposit small energy in the calorimeters due to minimum ionization. The energy deposition in the calorimeter increase linearity with muon momentum, and consequently the cut efficiency loss. To maintain good efficiency for high momentum muon, the cut is taken into account for the momentum dependence.

- Track-stub matching in $r-\phi$ plane($r \times \Delta\phi$) :

  The track is required to match the muon stub in $r-\phi$ plane.

4.2.3 Jet Reconstruction

Quark and gluon particles are observed as "jet" objects due to its fragmentation and radiation effects, as a results construct shower of particles. The energy of jet are calculated from the energy deposited in the calorimeter towers using a cone clustering algorithm with a fixed cone size in which the center of the jet is defined as (η^{jet}, ϕ^{jet}) and the size of the jet cone as $R = \sqrt{(\eta^{tower} - \eta^{jet})^2 + (\phi^{tower} - \phi^{jet})^2} = 0.4$. The jet clustering algorithm groups calorimeter towers with $E_{T_i} < 1$GeV. The algorithm is performed by first defining "Seed towers" has largest E_{T_i}. The seed tower are used to build "clusters" with size $R = 0.4$. The cluster transverse energy and its position is

calculated as the follows,

$$E_T^{jet} = \sum_{i=0}^{N} E_{T_i},\ \phi^{jet} = \sum_{i=0}^{N} \frac{E_{T_i}\phi_i}{E_T^{jet}},\ \eta^{jet} = \sum_{i=0}^{N} \frac{E_{T_i}\eta_i}{E_T^{jet}} \tag{4.6}$$

where N is the number of towers inside the radius R with $E_{T_i} > 1$GeV. This procedure is repeated until the cluster centroid is stable. Overlapping jets are merged if they overlap by more than 50%. If the overlap is smaller than 50%. each tower in the overlap region is assigned to the nearest jet. The measured jets are corrected to particle jet level or parent parton level by taking into account for the detector effects and for radiation and fragmentation effects. The collected jet transverse momentum is expressed as the follows,

$$\begin{aligned} p_T^{parton} &= (p_T^{jet} \times C_\eta - C_{MI}) \times C_{Abs} - C_{UE} + C_{OOC} \\ &= p_T^{parton} - C_{UE} + C_{OOC}, \end{aligned} \tag{4.7}$$

where p_T^{parton} is the transverse momentum of the parent parton, which is taken into account for all effects, p_T^{jet} is the transverse momentum measured in the calorimeter, p_T^{parton} is the transverse momentum of the particle jet, which is corrected for detector effects, and

- C_η is "η-dependent" correction. Thecorrection takes into account variations in calorimeter response and gain as a function of jet η
- C_{MI} is "Multiple Interaction" correction, which is the energy coming from multiple $p\bar{p}$ interaction in the same bunch crossing to subtract from the jet
- C_{Abs} is "Absolute correction", which is the correction of the calorimeter response to the momentum of the particle jet
- C_{UE} is "Underlying Event correction", to remove energy coming from underlying event such as initial state radiation and beam-beam remnant
- C_{OOC} is "Out-of-Cone correction", which is the correction of parton radiation and hadronization effects due to the finite size of the jet cone algotithm

The collections are performed by using the generic jet samples and MC samples generated by several generators(PYTHIA and HERWIG), and the systematic uncertainties coming from these collections also estimated. The systematic contribution mainly arise from the absolute jet energy collection due to difference between data and MC for calorimeter response(2%). The total systematic uncertainty is decreasing $\sim 8\%$ to $\sim 2\%$ as the jet energy increases(0 to > 80GeV).

4.2.4 Missing Transverse Energy

However neutrinos cannot be detected with CDF detector, its energy will manifest as missing energy. The CDF uses "missing transverse energy($\not\!\!E_T$)" taking into account for

transverse energy imbalance because of the missing energy, the vector sum of transverse energies should be ideal null. The missing transverse energy is measured using the transverse energy imbalance,

$$\not\!\!E_T = -\sum_i E_T^{(i)}, \tag{4.8}$$

where $E_T^{(i)}$ is the transverse energy of i-th calorimeter towar. It need to be corrected for the muon minimum ionization energy taking into account for muon momentum measured by tracking.

4.3 Like-Sign Dilepton Event Selection

The final desirableevents in this thesis are like-sign dilepton events to search for the supersymmetric particles. To collect the events, the series of selection as mentioned in § 3.2 are applied to the data corresponding to an integrated luminosity of 2.7fb^{-1}. In the selection, the applied transverse energy or momentum requirement to dilepton is asymmetric. If the 1st lepton is

- electron, $E_T > 20$ GeV and $p_T > 10$ GeV/c
- muon, $p_T > 20$GeV/c

while, if the 2nd lepton is

- electron, $E_T > 6$ GeV and $p_T > 6$ GeV/c
- muon, $p_T > 6$ GeV/c

where the 1st lepton type is required to match trigger path.

The selected dilepton events are applied more selection cuts to clean up the sample. The additional selections are listed in Table 4.2. The dilepton is required to be consistent with coming from the same vertex, which is an important requirement for dilepton and multi-lepton signatures. The dilepton mass cut is to reject onium events such as J/ψ or Υ. The Z removal($81 < M_{\ell\ell} < 101 GeV/c^2$) introduce to reduce WZ and ZZ events which potentially can be like-sign dilepton events in the final state. The Z-leg candidates are not the lepton passing lepton selection but also other object listed in Table 4.3 to catch Z events as many as possible. Finally, of course, like-sign charge combination requires to the dilepton events.

Electron selection	Muon selection
Event pre-selection	
$\lvert z_{\rm pv}\rvert < 60$cm	
Cosmic-ray veto	
Geometrical and kinematical cuts	
CEM	CMUP or CMX
Fiducial	Fiducial(CMUP), $\rho_{\rm COT} > 140$cm(CMX)
	Blue-beam veto, keystone veto, miniskirt veto
$E_T^{\ell_1} > 20$ GeV($p_T > 10$ GeV/c)	$p_T^{\ell_1} > 20$ GeV/c
$E_T^{\ell_1} > 6$ GeV($p_T > 6$ GeV/c)	$p_T^{\ell_2} > 6$ GeV/c
Track quality cuts	
Axial ≥ 3 and stereo $\geq$ (≥ 7 hits)	
$\lvert z_0 - z_{\rm pv}\rvert < 2$cm	
Silicon hits ≥ 3	
$\lvert d_0\rvert < 0.02$cm	
Isolation cut	
$\mathrm{ISO}_{0.4}^{\rm cal} < 2$ GeV	
Identification cuts	
HAD/EM $< 0.055 + 0.00045 \times E$	EM $<$ max(2, 2+0.0115$\times$($p - 100$)) GeV
$L_{\rm shr} < 0.2 (E_T < 70$ GeV)	HAD $<$ max(6, 6+0.0280$\times$($p - 100$)) GeV
$E/p < 2 (E_T < 50$ GeV)	$\lvert r \times \Delta\phi\rvert < 3, 5, 6$ cm (CMU, P, X)
$\chi^2_{strip} < 10$	
$\lvert\Delta_{z_{CES}}\rvert < 3$cm	
$-3.0 < Q \times \Delta_{x_{CES}} < 1.5$cm	
Other cuts	
Conversion removal	

Table 4.1: Event pre-selecion and lepton selection cuts.

Exactly two leptons
$\lvert z_0^{l_1} - z_0^{l_2} \rvert < 2$ cm
Dilepton mass > 12 GeV/c^2
Z removal
At least one like-sign pair

Table 4.2: Dilepton selection cuts.

Track object
Opposite-sign
$p_T > 10$ GeV/c
track coneisolation < 4 GeV/c
axial 3 and stereo 2 (5 hits)
$\lvert z_0 - z_{pv} \rvert < 10$ cm
EM object
$E_T > 10$ GeV
HAD/EM < 0.12
fractional isolation $\mathrm{ISO}_{0.4}^{cal}/E_T < 0.15$
Muon object
$p_T > 10$ GeV/c
EM < 5 GeV
HAD < 10 GeV
fractional isolation $\mathrm{ISO}_{0.4}^{cal}/p_T < 0.15$
$\lvert z_0 - z_{pv} \rvert < 10$cm
$\lvert d_0 \rvert < 0.5$cm

Table 4.3: Physics objects used to identify and remove Z bosons.

Chapter5

Background

Although the like-sign(LS) requirements are quit effective to supress QCD and known electroweak processes, fake-lepton backgrounds including non-prompt leptons such as those from photon conversions or from heavy-flavor decay, as well as literal fake leptons, still remain at a considerable level in the events of our signature. They are estimated by using data and MC samples, and the contributions of residual photon-conversion which survived our conversion veto are separated from the rest of the fake-lepton backgrounds by knowing the conversion detection efficiency and the number of identified conversions. While other backgrounds which is containing prompt real lepton are estimated by using MC data.

5.1 Fake Lepton

Fake leptons are one of major backgrounds in the LS deilepton events. They were estimated by weighting lepton + isolated track events with the expected fake-lepton yield for a given isolated track. These rates used to estimate fake-lepton backgrounds are called the fake-lepton rates, and are defined with respect to some reference rates, the rates of denominator objects. It is expected that the simple isolated-tracks in the opposite-sign(OS) combination are significantly contaminated by real leptons from Drell-Yan process, which leads to overestimates of fake-lepton backgrounds. To avoid this problem and to establish a consistent scheme which can be applied to both the OS and LS cases, we choose isolated tracks that deposits certain energies in the electromagnetic(EM) and Hadron(HA) calorimeters in the way such that they are not likely to be induced by real leptons.

5.1.1 Fake-lepton Backgrounds

The lepton plus fake-lepton backgrounds arise typically from a single lepton event such as $W \to \ell\nu$. This type of backgrounds consist of one trigger lepton and one fake lepton. The components of the "fake lepton" are

- **Fake lepton**
    1. Interactive $\pi^{\pm}$ →fake electrons,
    2. Overlap of π and a track → fake electrons,

3. Punch-through hadrons $\rightarrow$ fake muons,

- **Non-prompt leptons**

1. Residual photon conversions $\rightarrow$ electrons
2. Decay-in-flight muons from $\pi^{\pm}$ and $K^{\pm} \rightarrow$ muons,
3. (Semi-)Leptonic decay of heavy-flavour hadrons $\rightarrow$ leptons.

As noted here, we use "fake-leptons" as a generic word to mean both the literal fake leptons and non-prompt leptons. Most of the components are considered to be non-isolated and quite common in generic QCD events, while the residual photon-conversions are not necessarily QCD specific, and they are separately estimated from identified conversions with a similar philosophy as the fake-lepton rates. Correspondingly, contributions of residual conversions are subtracted from fake-electron rates in this study.

5.2 Residual Photon-conversions

The residual photon-conversion events arise from an electron originating from the photon conversion with an unobserved partner track due to its low momentum. The amount and kinematical shape of the events are estimated by multiplying lepton + conversion events by residual photon-conversion rate(R_{res}).

5.3 Physics Background

The physics backgrounds can be classified into reducible and irreducible backgrounds:

- **Reducible backgrounds**

1. $Z/\gamma^* \rightarrow \ell^+\ell^-$,
2. $W+$(heavy-flavor hadrons)$\rightarrow \ell\ell + X$,
3. $t\bar{t} \rightarrow (W^+b)(W^-\bar{b}) \rightarrow \ell\ell + X$,
4. $W^+W^- \rightarrow (\ell^+\nu)(\ell^-\nu)$

- **Irreducible backgrounds**

1. $WZ \rightarrow (\ell^{\pm}\nu)(\ell^+\ell^-)$,
2. $ZZ \rightarrow (\ell^+\ell^-)(\ell^+\ell^-)$.

The reducible backgrounds are reduced first of all by the LS requirement. When they contribute to LS dilepton events, the events are most likely due to residual conversions or fake leptons contained in these physics events, thus reduced also by the isolation cut. The irreducible backgrounds are supressed mainly by a Z veto at the first order.

Chapter6

Search for The SUSY Production

This section describes the sensitivity for chargino-neutralino production search using LS-dilepton events. This productions at CDF are shown in fineman diagram in Figure 6.1. In this thesis, we use MC samples to the search of the SUSY events. For the simulation of the production, we require the leptonic decay shown in Figure 6.2. Since the SUSY production have strong parameter dependence, we search for the events in varied parameter set.

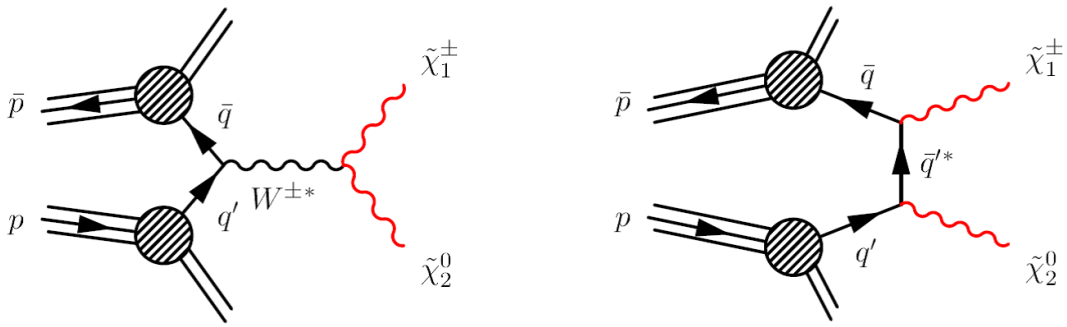

Figure 6.1: Chagino-Neutralino production at CDF.

6.1 Detection Efficiency and Event Yield

The detection efficiency and event yield after passing LS-dilepton selection are estimated by using SUSY MC which are generated by PYTHIA assuming mSUGRA parameter $M_{1/2}$ from 100 to 300 GeV/c^2 in 40 GeV/c^2 steps, for $M_0 = 60$ GeV/c^2, $A_0 = 0$, $\tan\beta = 5.0$, $\mu > 0$. The properties and the number of generated events for each MC is shown in Table 6.1. The expected event yield for $\tilde{\chi}_1^{\pm}\tilde{\chi}_2^0$ →LS-dilepton events are calculated by,

$$N = \upsilon(\tilde{\chi}_1^{\pm}\tilde{\chi}_2^0 \to \ell^{\pm}\ell^{\pm}) \cdot L \cdot \sigma(p\bar{p} \to \tilde{\chi}_1^{\pm}\tilde{\chi}_2^0), \tag{6.1}$$

where $\upsilon(\tilde{\chi}_1^{\pm}\tilde{\chi}_2^0 \to \ell^{\pm}\ell^{\pm})$ is the detection efficiency for $\tilde{\chi}_1^{\pm}\tilde{\chi}_2^0 \to \ell^{\pm}\ell^{\pm}$, L is the integrated luminosity, $\sigma(p\bar{p} \to \tilde{\chi}_1^{\pm}\tilde{\chi}_2^0)$ means the production cross section. The estimated values

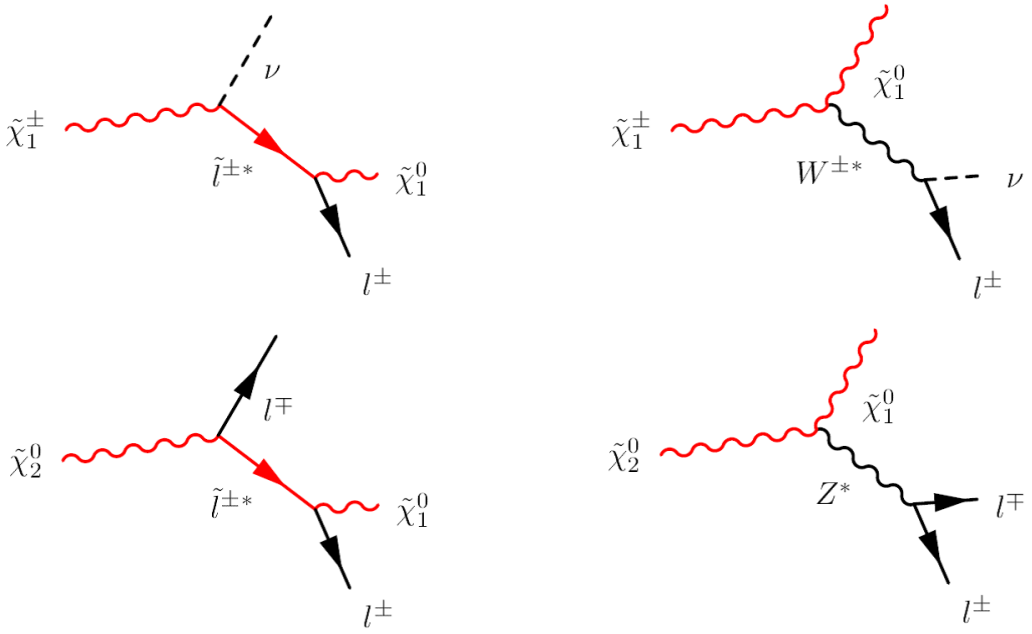

Figure 6.2: Requirement of Chagino-Neutralino decay.

are taken into account relevant scale factors. Table6.2 shows the detection efficiency and the expected event yield for each mSUGRA parameter space. The calculation of cross section and branching ratio are made with the packages "**SOFTSUSY**", "**SUSYHIT**" and "**PROSPINO**".

6.2 Multivariate Analysis

The search for smaller signal in larger data(background) has become essential to use the available information from the data as possible to get more search sensitivity. The multivariate data analysis can extract the maximum of the imformation. In this search, "Boosted Decision Trees(BDT)" technique which is one of the multivariate data analysis is employed. Decision trees is a binary tree structured classifier such as Figure6.3. "S" means signal, "B" means background, terminal nodes are called "leaves". The naming for S or B is depending on the majority of events in the each node. The tree structure is built up by repeatedly splitting the given events to regions that are eventually classified as signal or background. A shortcoming of decision trees has instability for classifier response due to statistical fluctuation in the samples, derives the tree, called training samples, for example if two input variables such E_T and p_T exhibit similar separation power, the variables are handled as almost like one variables. In such a case the whole tree structure is altered below this node. This problem is overcame by "Boosting"

$m_{1/2}$ (GeV/c^2)	$m_{\tilde{\chi}_1^\pm}$ (GeV/c^2)	$m_{\tilde{\chi}_2^0}$ (GeV/c^2)	$\sigma(p\bar{p} \to \tilde{\chi}_1^\pm \tilde{\chi}_2^0)$ (pb)	Generated Events
100	43	53	33.4	1921220
140	79	84	2.66	2289701
180	114	117	0.61	2310851
220	149	151	0.18	2380643
260	183	184	0.06	2388850
300	217	218	0.03	2363115

Table 6.1: SUSY Monte Calro samples.

$m_{1/2}$ (GeV/c^2)	Efficiency (%)	Expected Events
100	0.28	68 ± 4
140	0.97	48 ± 3
180	0.87	10.1± 0.6
220	1.02	3.2± 0.2
260	0.72	0.40± 0.03
300	0.87	0.33± 0.02

Table 6.2: Detection efficiency and expected event for SUSY passing LSDL selection.

algorithm. The Boosting constructs a forest of decision tree with modifies weights in event, as a result increases the statistical stability for the classifier and also improve the separation performance comparing with a single decision tree.

6.2.1 Decision Tree

The Decision Tree are built up the splitting criteria for each node. The splitting procedure is repeated until the whole tree is built. The split is determined by finding the variable and corresponding cut value that provides the best separation between signal and background. The node splitting is stopped at time that node is reached the required minimum number of events. The leaf nodes are classified as signal or background according to the majority of events in the node. The employed splitting criterion is "Gini-Index" to build the decision trees in this thesis. The Gini-Index is defined as

$$i_G = p(1-p), \tag{6.2}$$

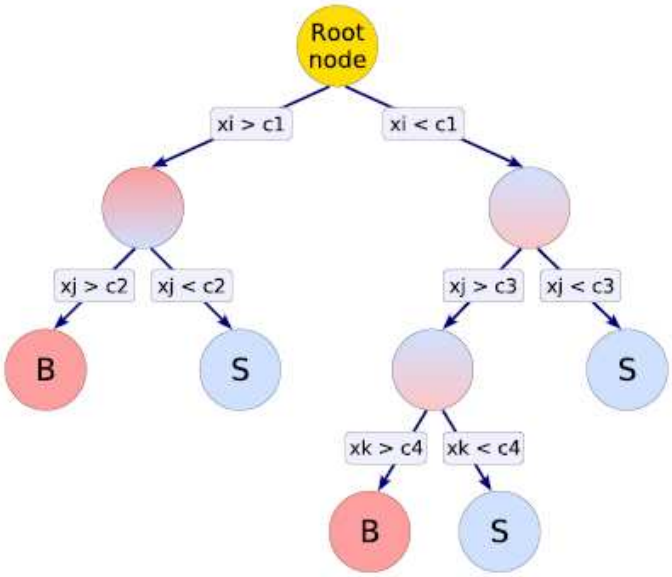

Figure 6.3: Schematic view of a decision tree.

p is purity in a node defined as follows,

$$p = \frac{\sum_s W_s}{\sum_s W_s + \sum_b W_b}, \tag{6.3}$$

where $\sum_s$ is the sum over signal evnts and $\sum_b$ is the sum over background events in a node, assuming the events are weighted with each events having W_i, so $p(1-p)$ is 0 if the samples is pure signal or pure background. The criterion is to maximize

$$i_G(\text{parent}) - i_G(\text{left-child}) - i_G(\text{right-child}), \tag{6.4}$$

where i_G(parent) means Gini index of a node before splitting(parent node), and i_G(left-child, or right-child) means Gini index of a node after splitting from parent node.

The maximum constructed decision tree has some statistically insignificant nodes which leads to reduce the separation performance(overtraining). Some "pruning" methods are used to avoid the overtraining as possible. "Cost-complexity pruning" is used to perform the maximum separation. The cost-complexity in a tree T starting at node t is expressed by

$$R_\alpha(T_t) = R(T_t) + \alpha \cdot N(T_t), \tag{6.5}$$

where, $R(T_t)$ is the total error cost in the tree T, the erroe cost in each terminal node is given by multiplying the $1 - max(p, 1-p)$ by the proportion of data, α is the cost complexity parameter, and $N(T_t)$ is the number of terminal nodes in the tree T, while the cost-complexity at node t is

$$R_\alpha(t) = R(t) + \alpha. \tag{6.6}$$

As long as $R_\alpha(t) > R_\alpha(T_t)$ the tree T has a smaller cost-coplexity than the single node t, in other words, it is worth to keep this node expanded. The inequality also expressed as the follows,

$$\alpha < \frac{R(t) - R(T_t)}{N(T_t) - 1}. \tag{6.7}$$

The node t with the α in the tree T is recursively pruned away as long as violating(6.7). Overtraining is managed by using the pruning method.

6.2.2 Boosting Algorithm

As described before, A single decision tree has instability for classifier response due to statistical fluctuation in the samples. In this thesis, "Adaboost" algorithms are used to overcom the problem, which is one of the some boosting algorithms. In general, the training events which were misclassified have their weights increased i.e. boosted, and new tree is formed. This procedure is then repeated for the new tree, as results many trees are built up. The score from the mth individual tree T_m is taken as $+1$ if the events falls on a signal leaf and -1 if the event falls on a background leaf. The final score is taken as a weighted sum of the scores of the individual leaves.

Suppese that there are N events in the samples. The events are assigned the weight $1/N$ at first. Some notations are defined as the follows,

- x_i is the set of information(for example p_T or E_T) for the ith
- $y_i = 1$ if the ith event is a signal event and $y_i = -1$ if the ith event is a background event
- w_i is the weight of the ith event
- $T_m(x_i) = 1$ if the set of information for the ith event lands that event on a signal leaf and $T_m(x_i) = -1$ if the set of information for that event lands on a background leaf.
- $I(y_i \neq T_m(x_i)) = 1$ and $I(y_i = T_m(x_i)) = 0$

where m is index for Mth tree. Using the above notations, define the misclassification rate error,

$$err_m = \frac{\sum_{i=1}^{N} w_i I(y_i \neq T_m(x_i))}{\sum_{i=1}^{N} w_i}, \tag{6.8}$$

The error is used to change the weight of each event

$$\alpha_m = \beta \times \ln(\frac{1 - err_m}{err_m}), \tag{6.9}$$

$$w_i \rightarrow w_i \times e^{\alpha_m I(y_i \neq T_m(x_i))}. \tag{6.10}$$

where $\beta = 1$ is the standard Adaboost method. The change weights are normalized to

$$w_i \to \frac{w_i}{\sum_{i=1}^{N} w_i}, \tag{6.11}$$

The score for a given event is

$$T(x) = \sum_{m=1}^{M} \alpha_m T_m(x), \tag{6.12}$$

which is the weighted sum of the scores of the individual trees. The boosting algorithm remedies the statistical fluctuation in the samples and improves the separation performance between signal and background. The BDT framework is implemented in TMVA package intefrated in ROOT framework, which is used in this search.

6.2.3 BDT Training Samples

There are two main background events for LS dilepton events. One background event is residual-photon conversions event, which is electron originated from photon conversion with unobserved partner track. The othe main background is fake leptons event. The components of the fake-lepton are interactive $\pi^{\pm}$, overlap of π^0 and a track, punch-through hadrons, and non-prompt leptons. The BDT descriminant is optimized to well separate between the higgs and the two main background, so-called "trining". The signal training samples are SUSY MC samples as shown in Table6.1, while background samples are residual-photon conversion events, and fake lepton events, which are derived from data samples. The training are performed by using each SUSY mSUGRA parameter space sample with the main background, independently. These samples are passing LS-dilepton selection criteria.

6.2.4 BDT Input Variables

The BDT is insensitive to insensitive to including input variables with low separation powers, because the ptuning procedure remove the splitting nodes under such variables, while the other multivariate technique have to carefully select the input variables and deal with it, for example Artificial Neural Network. If a strongly correlated variables is selected as inputvariable, the input variables to construct BDT discriminant.

- 1st lepton p_T (p_{T1})
- 2nd lepton p_T (p_{T2})
- vector sum of p_{T1} and p_{T2} (p_{T12})
- Missing E_T ($\not{E}_T$)
- Dilepton mass

- Number of jets($E_T > 15$GeV)
- MetSpec
  : $\not\!\!E_T$ if $\Delta\phi(\not\!\!E_T, \ell \text{or} jet) > \frac{\pi}{2}$
  : $\not\!\!E_T \sin(\Delta\phi(\not\!\!E_T, \ell \text{or} jet))$ if $\Delta\phi(\not\!\!E_T, \ell \text{ or } jet) < \frac{\pi}{2}$
- H_T : Sum of E_{T1}, E_{T2}, jets E_T and Missing E_T
- Sphericity

The normalized 9 input variables for LS-dilepton event are shown in Figure 6.5 and 6.4. The resaltant BDT score distributions for the each SUSY mSUGRA parameter spaces are shown in Figure6.6.

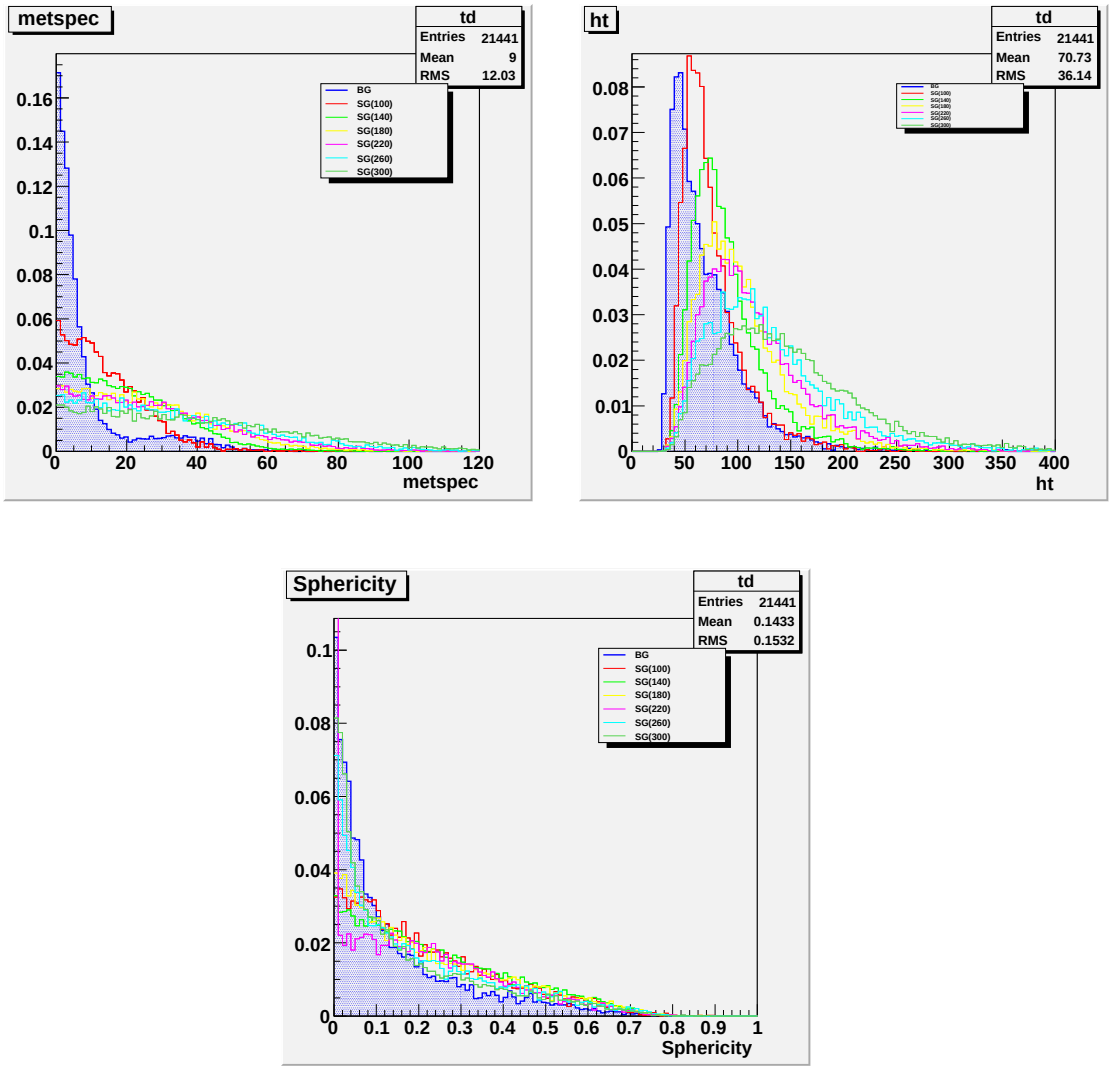

Figure 6.4: BDT input variables for MetSpec, H_T and Sphericity.

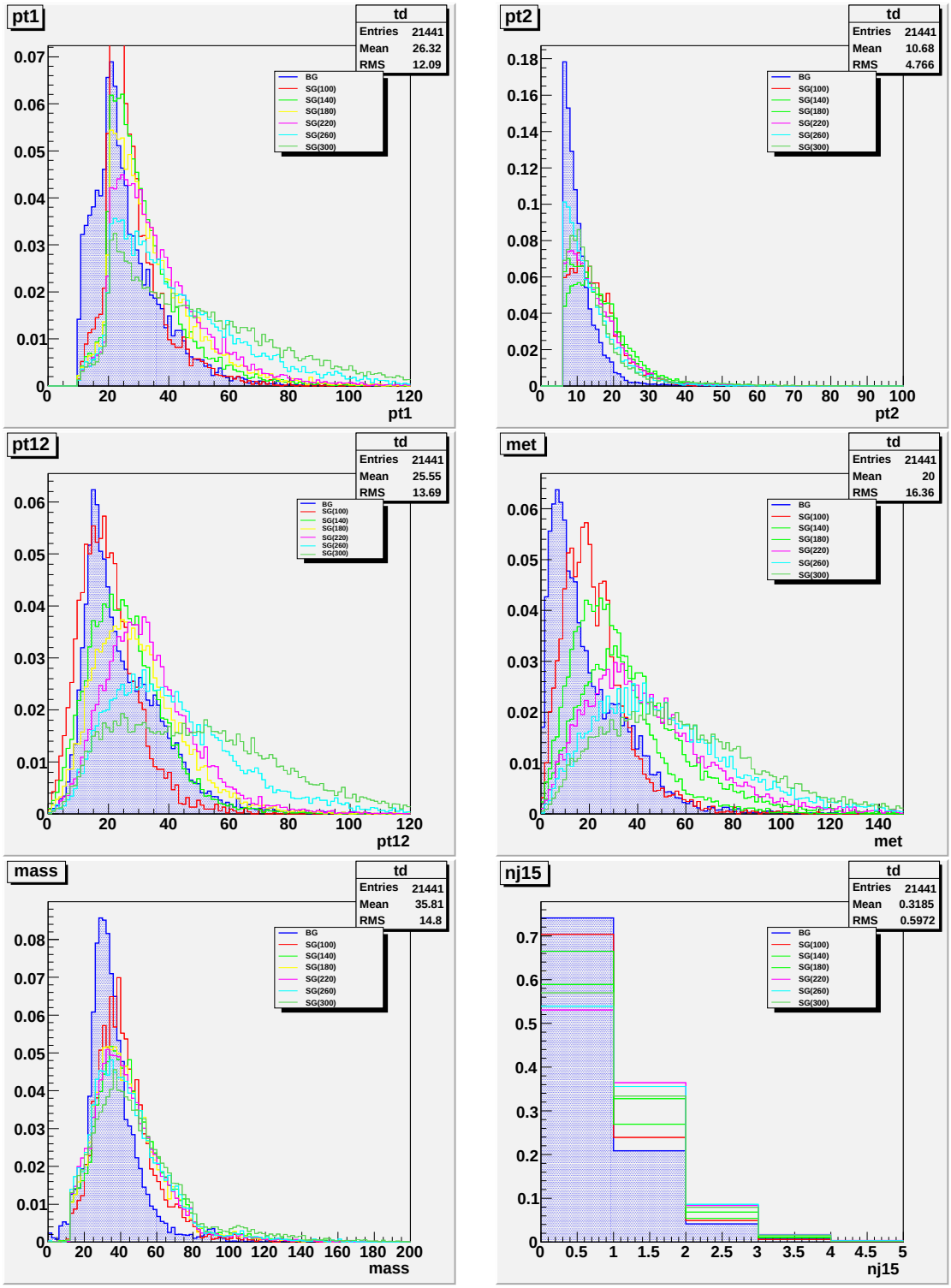

Figure 6.5: BDT input variables for p_{T1}, p_{T2}, p_{T12}, $\not{E}_T$, Dilepton mass and # of jet.

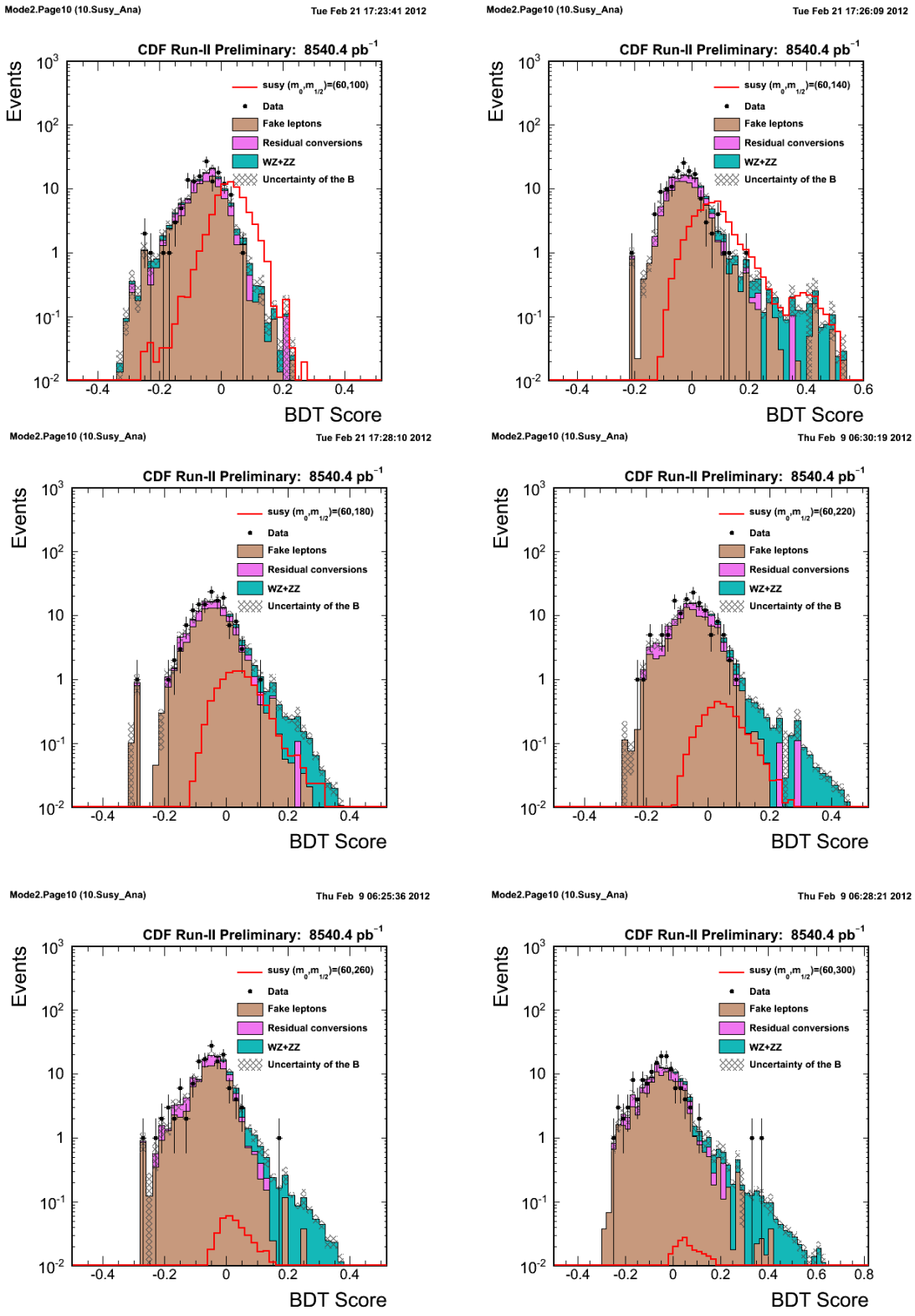

Figure 6.6: BDT output for like-sign dilepton ($M_{1/2}$ = 100, 140, 180, 220, 260 *and* 300 GeV/c^2).

Chapter7

Cross Section Upper Limit

7.1 Likelihood Function

The upper limit on production cross section is calculated by using Bayesian approach with fitting binned likelihood to the BDT output. The likelihood is constructed under the Poisson statistics:

$$p(\mu, n) = \frac{\mu^n e^{-\mu}}{n!}, \ \mu = s + b \tag{7.1}$$

where n is number of observed events, μ is expected number of events, and $s(b)$ is expected number of events for signal(background). In this thesis, the binned likelihood fitting to N bins histograms is written as follows,

$$\mathcal{L} = \prod_{k}^{N_{bin}} \frac{\mu^{n_k} e^{-\mu_k}}{n_k!}, \ \mu_k = s_k + b_k \tag{7.2}$$

In addition, the likelihood is taken some informations, the systematic uncertainties, into account by Gaussian,

$$\begin{aligned} \mathcal{L}(\sigma_1, \cdots, \sigma_{N_{proc}}; \delta_1, \cdots, \delta_{N_{syst}}) &= \prod_{k=1}^{N_{bin}} \frac{\mu_k^{n_k} \cdot e^{-\mu_k}}{n_k!} \\ &\quad \cdot \prod_{i=1}^{N_{proc}} G(\sigma_i | \sigma_i^{SM}, \Delta\sigma_i^{SM}) \cdot \prod_{j=1}^{N_{syst}} G(\delta_j | 0, 1) \end{aligned} \tag{7.3}$$

where N_{proc} is number of physics processes, N_{syst} is number of systematic sources. The expected event μ_k is taken both systematic uncertainties into account, expressed as the follows,

$$\mu_k = \sum_{i=1}^{N_{proc}} \mu_{ik} \cdot \delta_i^{rate} \cdot \delta_{ik}^{shape}, \tag{7.4}$$

$$\delta_i^{rate} = \prod_{j=1}^{N_{syst}} [1 + |\delta_j| \cdot \{\upsilon_{ij+} H(\delta_j) + \upsilon_{ij-} H(-\delta_j)\}] \tag{7.5}$$

$$\delta_{ik}^{shape} = \prod_{j=1}^{N_{syst}} [1 + |\delta_j| \cdot \{\kappa_{ijk+} H(\delta_j) + \kappa_{ijk-} H(-\delta_j)\}] \tag{7.6}$$

where υ_{ij} is the relative acceptance uncertainties from jth systematic source in ith process, κ_{ijk} is the relative uncertainty in the kth bin content from jth systematic

source in ith process. Heaviside step function $H(\delta_j)$ is used in the above equations, defined as the follows,

$$H(\delta_j) = \begin{cases} 1 \ (\delta_j > 0) \\ 0 \ (\delta_j < 0) \end{cases} \tag{7.7}$$

The likelihood function (7.3) is used to calculate the upper limit on production cross section $\sigma(p\bar{p} \to \tilde{\chi}_1^{\pm}\tilde{\chi}_2^0)$ at 95% confidence level.

7.2 Upper Limit at 95% Confidence Level

In this search, there is no significant excess in between data and background expectation, so the upper limits on production cross section $\sigma(p\bar{p} \to \tilde{\chi}_1^{\pm}\tilde{\chi}_2^0)$ at 95 % confidence level(C.L.) is set by using the binned likelihood function (7.3) in Bayesian approach with BDT output distribution as the following function,

$$0.95 = \frac{\int_0^{\sigma_{95\%}} \mathcal{L}(\sigma)d\sigma}{\int_0^{\infty} \mathcal{L}(\sigma)d\sigma}. \tag{7.8}$$

The upper limits are calcurated for observed ones corresponding to SUSY on $M_{1/2}$ =100 to 300 GeV/c^2 mSUGRA parameter space. Figure 7.2 shows the 95% observed cross section upper limit for the chargino-neutralino production on each mSUGRA parameter space par cross section of thory. And the relative upper limits to SUSY prediction cross section are also caluculated in Figure 7.2 as a function of chargino mass according to each mSUGRA parameter set.

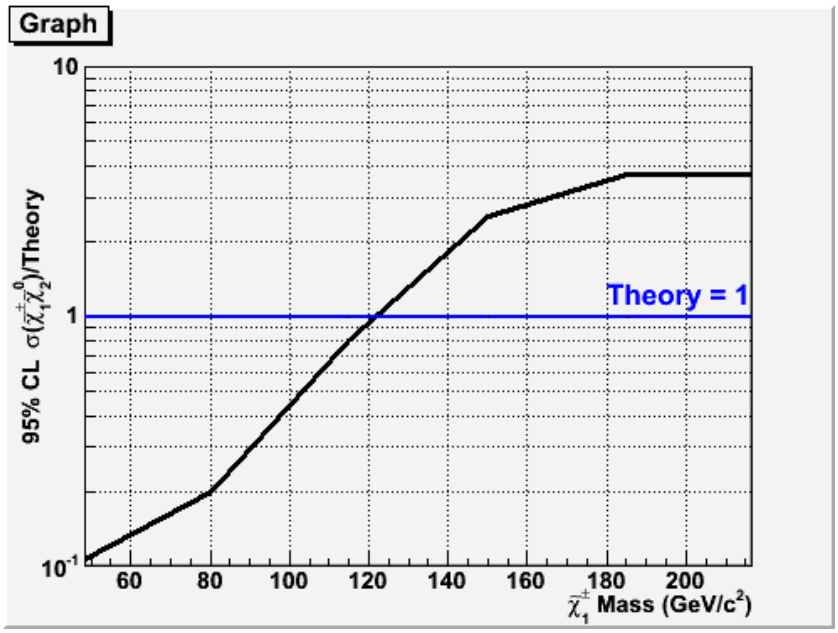

Figure 7.1: The relative upper limits as a function of chargino mass.

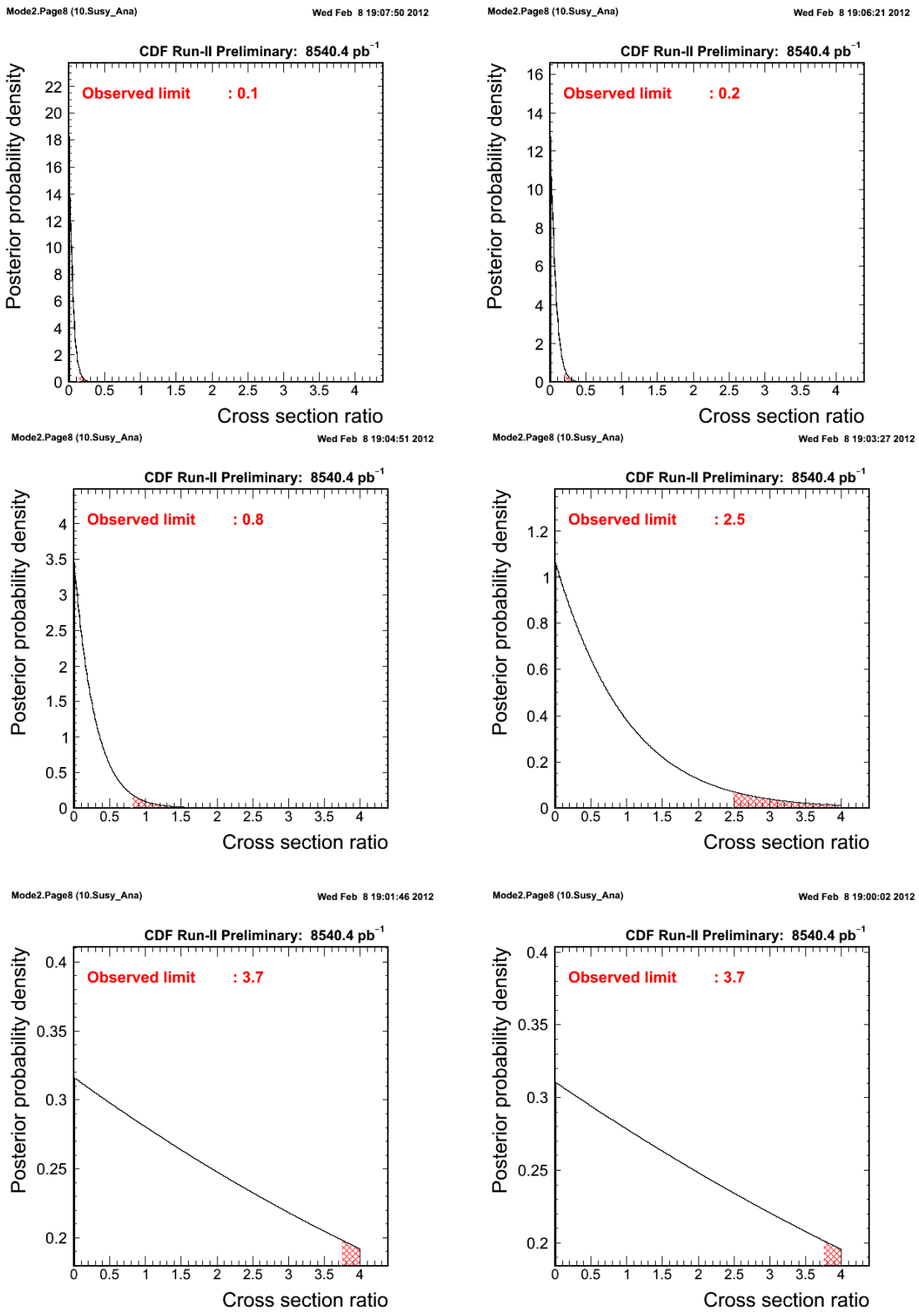

Figure 7.2: Cross Section Upper Limit for SUSY ($M_{1/2}$ = 100, 140, 180, 220, 260 *and* 300 GeV/c^2).

Chapter8

Conclusion

This thesis has described the search for the chargino-neutralino pair production using high-p_T like-sign dilepron events with the data corresponding to an integrated luminosity of 8.5fb^{-1}. The expected number of signal for the mSUGRA parameter set $(M_0, A_0, tan\beta, sign(\mu)) = (60GeV/c^2, 0, 5, +)$, was 68 for $M_{1/2} = 100GeV/c^2$ and 0.33 for $M_{1/2} = 300GeV/c^2$.

The Boosted Decision Tree technique was used to give more separation power between backgrounds and signal events in the final sample. From the BDT output distributions, there is no significant excess in between data and background expectation. So the upper limits on the production cross section $\sigma(p\bar{p} \to \tilde{\chi}_1^{\pm}\tilde{\chi}_2^0)$ at 95% confidence level was set by using the binned likelihood function in Bayesian approach with BDT output distribution. The observed limit for $M_{1/2}$ at 100 to 300 GeV/c^2 were respectively,

- $M_{1/2} = 100$ GeV/c^2 : $\sigma(p\bar{p} \to \tilde{\chi}_1^{\pm}\tilde{\chi}_2^0)/(\text{Theory}) < 0.1$
- $M_{1/2} = 140$ GeV/c^2 : $\sigma(p\bar{p} \to \tilde{\chi}_1^{\pm}\tilde{\chi}_2^0)/(\text{Theory}) < 0.2$
- $M_{1/2} = 180$ GeV/c^2 : $\sigma(p\bar{p} \to \tilde{\chi}_1^{\pm}\tilde{\chi}_2^0)/(\text{Theory}) < 0.8$
- $M_{1/2} = 220$ GeV/c^2 : $\sigma(p\bar{p} \to \tilde{\chi}_1^{\pm}\tilde{\chi}_2^0)/(\text{Theory}) < 2.5$
- $M_{1/2} = 260$ GeV/c^2 : $\sigma(p\bar{p} \to \tilde{\chi}_1^{\pm}\tilde{\chi}_2^0)/(\text{Theory}) < 3.7$
- $M_{1/2} = 300$ GeV/c^2 : $\sigma(p\bar{p} \to \tilde{\chi}_1^{\pm}\tilde{\chi}_2^0)/(\text{Theory}) < 3.7$

From this results, we could exclude the mSUGRA region for the chargino mass < 120 GeV/c^2.

Bibliopraphy

[1] Francis Halzen and Alan D. Martin, "Quarks and Leptons: An Introductory Course in Modern Particle Physics" John Wiley & Sons

[2] Lewis H. Ryder "Quantum Field Theoty" Cambridge University Press

[3] C. Amsler *et al*(Particle Data Group), "Review of Particle Physics", Phys. Lett. B

[4] S. Glashow, "Partial Symmetric of Weak Interactions", Nucl. Phys.

[5] A. Salam "Elementary Particle Theory", ed N. Svartholm, Almqvist and Wiksells, Stockholm

[6] M. Drees "Theory And Phenomenology of Sparticles: An Account of Four-dimensional N=1 Supersymmetry in High Energy Physics"

[7] Ian J.R. Aichison, AJ.G. Hey, "Gauge Theory in Particle Physics Volume 1: From Relativistic Quantum Mechanics to QED" Taylor & Francis.

[8] Donald H. Perkins, "Introduction to High Energy Physics 4th edition" CAMBRIDGE

[9] Stephen P. Martin, "A Supersymmetry Primer" arXiv:hep-ph/9709356

[10] Ian Aitchison, "Supersymmetry in particle Physics: An Elementary Introduction" Cambridge University Press

[11] S. Dawson "SUSY AND SUCH" arXiv:hep-ph/9612229v2

[12] T. Wakisaka "Search for the Wh Production Using High-p_T Isolated Like-Sign Dilepton Events in 1.96-TeV Proton-Antiproton Collisions", World Scientific Pub Co inc

[13] The CDF II Collaboration, "The CDF II Detector Technical Design Report",

[14] T.K. Nelson *et al*, "The CDF Layer 00 Detector", FERMILAB-CONF-01/375-E

[15] C.S. Hill *et al*, "Initial experience with the CDF layer 00 silicon detector", Nucl. Instrum. and Meth.

[16] A. Sill *et al*, "CDF Run II silicon tracking projects", Nucl. Instrum. and Meth.

[17] W. Ashmanskas *et al*, "The CDF silicon vertex trigger", Nucl. Instrum. and Meth

[18] A. Affolder *et al*, "Status report of the Intermediate Silicon Layers detector at CDF II", CDF public Note

[19] A. Affolder *et al*, "Instermediate silicon layers detector for the CDF experiment", Nucl. Instrum. and Meth.

[20] T.Affolder *et al*, "CDF Central Outer Tracker", CDF Public Not 6267

[21] L. Balka *et al*, "The CDF Central Electromagnetic Calorimeter", Nucl. Instrum. Meth.

[22] D. Acosta *et al*, "The CDF Cherenkov luminosity monitor", Nucl. Instrum. Meth.

[23] H. Yang, B.P.Roe and J.Zhu. "Studies of Boosted Decision Trees for MiniBooNE Particle Identification", arXiv:physics/0508045

[24] L.Breiman, J.H.Friedman, R.A.Olshen and C.J.Stone "Classification and regression trees", ISBN: 0-412-04841-8

[25] CDF Collaboration, D. Acota, *et al*, "Search for Electroweak single-top-quark production in $p\bar{p}$ collisions at $\sqrt{s} = 1.96$TeV", Phys. Rec.D71,012005

[26] The CDF Collaboration, "Searches for Associated Production of Chargino-Neutralino Pair in a Di-electron + Track Channel"

[27] Gordon Kane, "SUPERSYMMETRY: Univeiling the Ultimate Laws of Nature"

[28] P.Skands, B.C.Allanach *et al*, "SUSY Les Houches Accord: Interfacing SUSY Spectrum Calculators, Decay Package, and Event Generators" (http://home.fnal.gov/skands/slha/)